Journal of Wind Engineering & Industrial Aerodynamics 207 (2020) 104437

Contents lists available at ScienceDirect

Journal of Wind Engineering & Industrial Aerodynamics

journal homepage: www.elsevier.com/locate/jweia

On the reliability of the 3D steady RANS approach in predicting microscale wind conditions in seaport areas: The case of the IJmuiden sea lock

A. Ricci [a,b,c,*], B. Blocken [a,c]

[a] Unit Building Physics & Services, Department of the Built Environment, Eindhoven University of Technology, Eindhoven, the Netherlands
[b] Department of Civil, Chemical and Environmental Engineering, University of Genoa, Genoa, Italy
[c] Building Physics and Sustainable Design, Department of Civil Engineering, KU Leuven, Leuven, Belgium

ARTICLE INFO

Keywords:
Seaport areas
Microscale wind conditions
On-site measurements
Computational fluid dynamics (CFD)
Validation

ABSTRACT

Coastal areas and seaport areas are exposed to high wind speeds which may involve risks for the ships and people working in the area. Therefore, knowledge of the microscale wind conditions is essential for safe maneuvering and mooring of ships and optimizing harbor design. In the present study, 3D steady RANS CFD simulations with the realizable k-ε turbulence model are performed for the *new configuration* of the *"IJmuiden sea lock"* in Amsterdam, the largest sea lock in the world at the time of writing this article. The computed wind speed and turbulence intensity amplification factors and the local wind directions are validated with on-site measurements for the *old configuration* of the sea lock. For the wind speed amplification factor and local wind direction, a satisfactory agreement is obtained with 90% of CFD data within ±30% from the measured data. Conversely, for the turbulence intensity amplification factor, less satisfactory agreement is found with 74% of CFD data within ±30% from the measured data. Overall, the 3D steady RANS approach shows a sufficiently high reliability for predicting the wind conditions in the seaport area under neutral atmospheric conditions.

1. Introduction

Ports areas are important nodes and facilitate a large portion of the worldwide trade volume via sea. These areas can be considered in many cases the entry and the exit points of a country's trade (Kron, 2013). The total gross weight of goods handled in the European Union (EU) ports was estimated at 3.6 billion tons in 2018 and the Netherlands remained the largest maritime freight transport country in Europe in 2018. In 2018 the maritime transport counted about 415 million passengers embarking and disembarking in European ports alone and, with almost 85 million passengers passing through its ports, Italy was the major seaborne passenger country in Europe (Eurostat Statistics Explained, 2020). Ports are key players in the global trade and strategic nodes in the global supply chains (Yip, 2008; Rodrigue and Notteboom, 2009; Becker et al., 2015; UNCTAD, 2018; Vairetti et al., 2019). However, a large number of activities usually carried out in these areas (e.g. transport of passengers, transport of cargo, storage of oil and chemicals, storage and transport of vehicles, circulation of vessels and ships, lorries and trains) also imply high risks for human beings (Ronza et al., 2009; Fabiano et al., 2010; Cho et al., 2018). The consequences of accidents in port areas may be not only economic losses (e.g. for emergency actions and cleaning up the areas) but also human losses (Ronza et al., 2009).

For historical and practical reasons approximately 3 billion people have settled within 200 km of coastal areas (Population Reference Bureau, 2003). There is a large number of European cities either placed inland and closely linked to their own port by waterways (mainly North European ports such as Rotterdam and Antwerp) or directly located on the coastline and equipped with a port (mainly Mediterranean ports such as Genoa and Marseille) (Darbra and Casal, 2004). In both cases these *"hybrid areas"*, most commonly called *"seaports"*, can be considered as an example of large-scale infrastructure indispensable to the global trade (McIntosh and Becker, 2019). However, due to the presence of a large number of people, possible accidents in these environments can have serious consequences. Darbra and Casal (2004) carried out an interesting statistical analysis on 471 historical accidents that occurred in seaports from 1941 to 2002, and they found that 56.5% of these occurred during transport operations (i.e. moving ships) and 43.5% of these occurred during various types of on-shore/off-shore operations, such as loading and unloading goods and the storing process. Then, the main causes of these accidents were grouped into four categories (i.e., impact, mechanical failure, external events and human factor) and high wind speed was found to be a significant contributor with 4%, 7% and 25% of

* Corresponding author. Unit Building Physics & Services, Department of the Built Environment, Eindhoven University of Technology, Eindhoven, the Netherlands.
E-mail address: a.ricci@tue.nl (A. Ricci).

https://doi.org/10.1016/j.jweia.2020.104437
Received 10 August 2020; Received in revised form 31 October 2020; Accepted 31 October 2020
Available online 18 November 2020

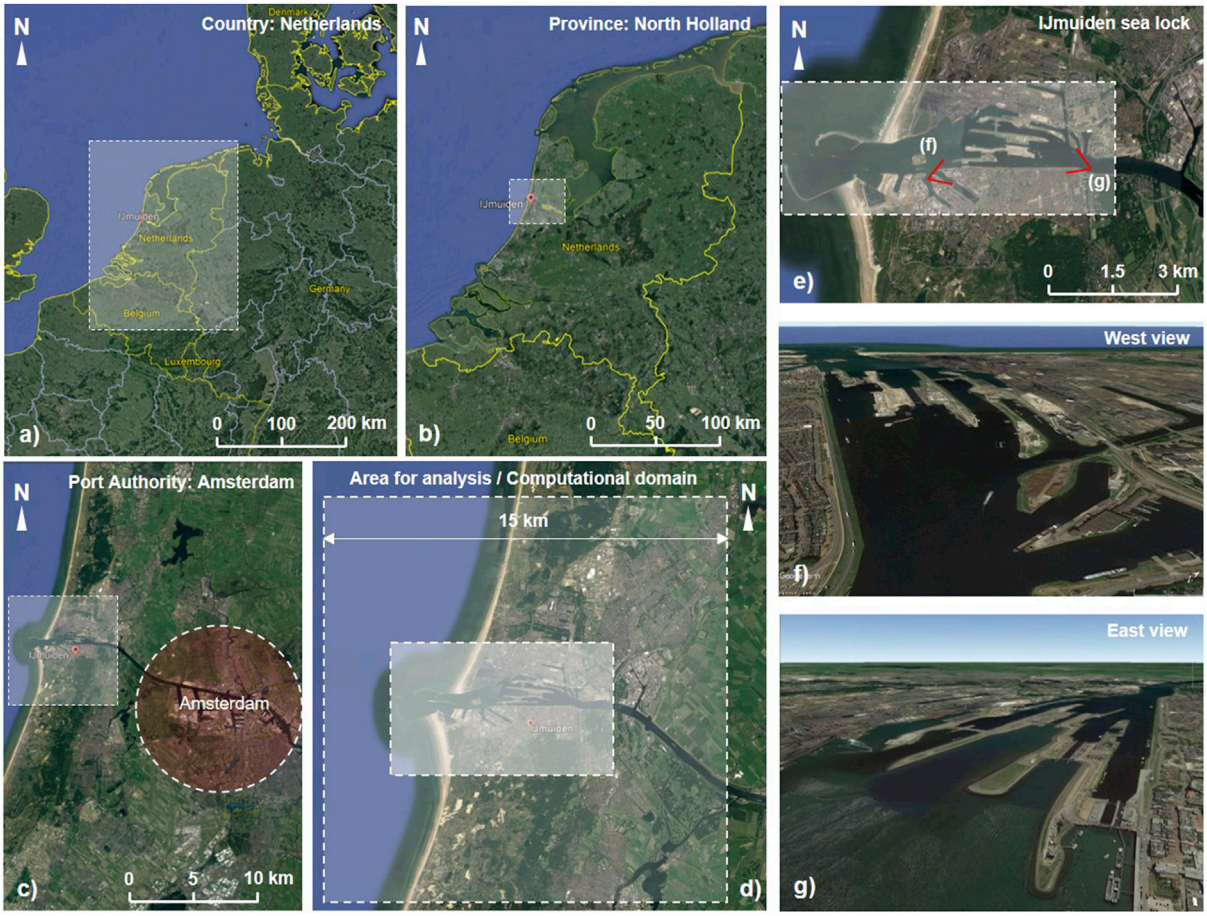

Fig. 1. Geographical location of the study area. Photos credit to *Google Maps*.

occurrence in the first three groups, respectively. Nevertheless, this is not surprising for the wind engineering community. It is well-known that coastal areas experience more intense and more frequent natural events such as strong winds (Kron et al., 2019) since they can be considered the *"first point of contact"* between the open sea (where wind speeds can be very high) and the inland (where the wind speed decreases due to the higher roughness of the surface of the Earth). Therefore, seaport areas and more generally coastlines may be considered among the most risky areas in the world, since at these locations catastrophes frequently happen, people die and their properties are destroyed (Kron, 2013).

Among geophysical events (e.g. earthquakes), meteorological events (e.g. wind storms), hydrological events (e.g. floods) and climatological events (e.g. droughts), the wind is considered to be the prime cause in terms of economic and human losses in seaport areas (Solari et al., 2012; Tamura and Cao, 2012; Kron, 2013; Ulbrich et al., 2013; Zhang and Lam Siu Lee, 2015; Taramelli et al., 2015; Repetto et al., 2017, 2018; Kantamaneni et al., 2019). Three of the main global trade partners, the Netherlands (where the present project takes place), Belgium and the United Kingdom, still preserve memories about the biggest sea-related catastrophe that ever happened in Northern Europe. On the night of January 31 – February 1, 1953, a combination of a spring tide and a strong wind blowing from the North Sea caused a storm surge on the coastline of these three countries, killing 2551 people and causing billions of euros of losses (Nederlands Instituut voor Beeld en Geluid, 1953; Kron et al., 2019). Since then, the Netherlands as well as other Northern European countries with the biggest seaport areas (e.g. the United Kingdom, Belgium, Germany and Denmark) spent billions of euros to strengthen and build *"sea defense systems"*. However, a new challenge has emerged for ports that have to face the competition of emerging ports worldwide (Cho et al., 2018). The size of seaport infrastructures (Cho et al., 2018) as well as of container ships (Gomez Paz et al., 2015; Merk, 2015; Martin et al., 2015; van Hassel et al., 2016; Malchow, 2017; Lu and Yeh, 2019) and cruise ships (Sun et al., 2014; Bucci et al., 2016; Castillo-Manzano and Lopez-Valpuesta, 2018) has increased significantly over the last decades. The increasing ship size does not only cause larger wind forces but also larger ship inertia, which renders the navigation through the port areas even more difficult, especially on windy days (Blocken et al., 2015; Janssen et al., 2017; UNCTAD/RTM/2018; Rong et al., 2019; Torre et al., 2019; Ricci et al., 2020a; Wang and Wan, 2020; Wang et al., 2020). In this regard, the knowledge of macroscale and microscale wind conditions is essential for safety management, for maneuvering and mooring of ships (Blocken et al., 2015; Janssen et al., 2017; Donatini et al., 2019; Ricci et al., 2020a), for optimizing the harbor design and also for reducing economic losses associated with port disruption due to extreme wind events (Solari et al., 2012; 2020; Burlando et al., 2014, 2017a,b; Zhang and Lam Siu Lee, 2015; Becker et al., 2015; Mori and Takemi, 2016; Cao and Siu Lee Lam, 2018; Jian et al., 2019). Many studies on the prediction of macroscale and microscale wind conditions over coastal and seaport areas have been carried out in the last decades. The majority of these were performed by on-site measurements, forecasting models and Numerical Weather Prediction (NWP) (e.g. Burlando et al., 2007; Katinas et al., 2009; Al-Yahyai et al., 2010; Walsh et al., 2012; Solari et al., 2012; Cassola and Burlando, 2012; Burlando et al., 2013; Burlando et al., 2014; Oner et al., 2013; Donateo et al., 2014; Repetto et al., 2017; 2018; Mathias et al., 2019; Arslan et al., 2020). In contrast, to the best knowledge of the authors, only a very

Fig. 2. Photographs taken at different positions of the *old configuration (2015)* of the *IJmuiden sea lock:* (*a*) indication of positions and viewing direction: (*b*) *Steigerweg*, (*c*) *Harlingenstraat*, (*d*) *Noordersluisweg* 1, (*e*) *Noordersluisweg*, (*f*) *Binnenspuikanaal* and (*g*) *Noordersluisweg*. Photograph (*h*) shows the area of the old configuration of the sea lock (2015) indicated with the dashed rectangle in figure (*a*) with indication of the six locks of the port. Photos (*a*) and (*b*) credit to *Google Maps*.

limited number of these studies were performed by Computational Fluid Dynamics (CFD) and/or by a combination of CFD with on-site measurements (e.g. Blocken et al., 2015; Ricci et al., 2020a). CFD is the only numerical method capable of resolving also the local-scale effects induced by individual obstacles such as buildings and ships by high-resolution computational grids. Within CFD, the steady Reynolds-averaged Navier-Stokes (RANS) approach is the most commonly used approach in wind engineering research and practice (Stathopoulos, 2002; Hanjalic, 2005; Baker, 2007; Franke et al., 2007; Blocken 2014, 2018). Nevertheless, it is still insufficiently known to what extent the 3D steady RANS approach can be accurate and reliable for predicting the wind conditions in *"seaport areas"* in which an *"urban area"* and a *"port"* are combined. Such areas are generally characterized by a wide range of different aerodynamic roughness lengths (e.g. sea versus densely built-up harbor docks) and by numerous strong changes in surface roughness (e.g. from harbor basins to adjacent docks with container stacks and back to harbor basins, and so on).

Therefore, the objective of the present paper is to analyze the reliability of the 3D steady RANS approach for predicting the microscale wind conditions in a seaport area. The area under study is the *IJmuiden sea lock*, in Netherlands, and the surrounding built environment. Although the present study focuses on a specific seaport area located in Europe, the methodology and conclusions also pertain to similarly complex urban environments worldwide. At the time of writing this article, this sea lock was the largest in the world. The CFD simulations were carried out for 24 reference wind directions (θ) assuming neutral atmospheric conditions. Four 2D ultrasonic anemometers were installed recording from July 2017 to July 2018 and the CFD simulation results were compared to the measurements in terms mean wind speed (U), turbulence intensity (I) and local wind direction (φ). The paper is organized as follows. Section 2 contains a description of the case study and the problem statement. In Section 3, the on-site measurements are described. In Section 4 the computational geometry, domain, grid, the boundary conditions and other numerical settings are outlined. Section 5 presents the CFD results and the comparison between simulated and measured data. Finally, Section 6 concludes the paper.

2. Case study and problem statement

The *IJmuiden sea lock* resides under the Port Authority of Amsterdam

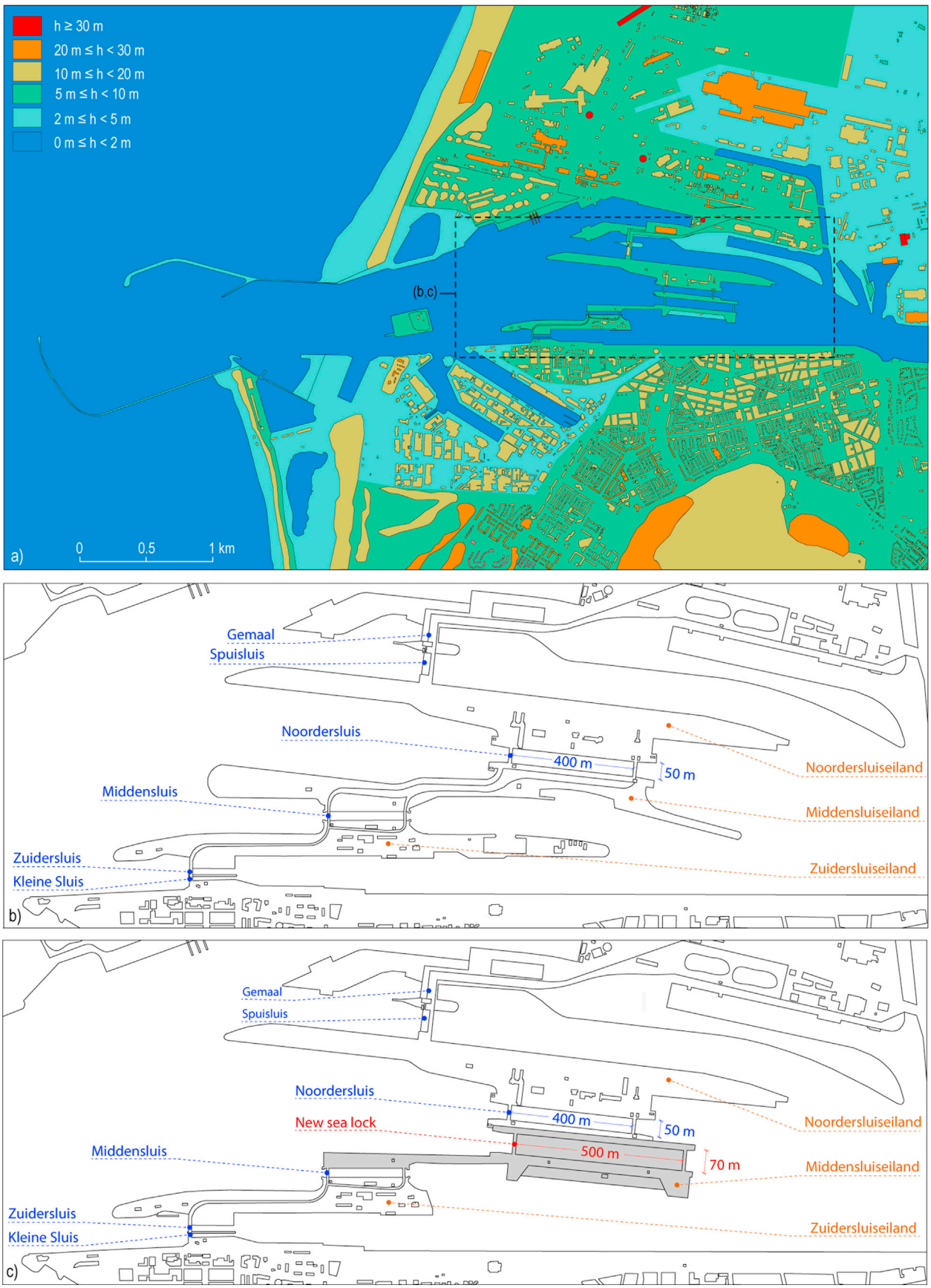

Fig. 3. Maps of the area under investigation indicating (*a*) six different ranges of altitude above mean sea level (MSL), (*b*) the *old configuration (2015)* and (*c*) the *new configuration (2022)* of the *IJmuiden sea lock*.

Fig. 4. Comparison among the (*a*) old configuration of sea lock (2015), (*b*) new configuration of the sea lock at the beginning of the construction (2017), (*c*) a recent status of the sea lock construction (2019). Photos credit to *Google Earth*.

Fig. 5. Positions of the 2D ultrasonic anemometers installed in the *IJmuiden sea lock*. Also the anemometer station of the *Royal Dutch Meteorological Institute* (KNMI) is shown. Top view photo credit to *Google Maps*.

in the province North Holland in the Netherlands (Fig. 1). IJmuiden is a seaport area located at the mouth of the North Sea Canal to Amsterdam and it is a main town in the municipality of Velsen. The selected study area extends from UTM 52°32′16″ N - 4°42′34″ E to 52°24′38″ N - 4°28′23″ E (Fig. 1d) and covers 225 km^2 (15 × 15 km^2). It encompasses nine municipalities (i.e. *Velsen, Beverwijk*, *Heemskerk*, *Castricum*, *Uitgeest*, *Zaanstad*, *Haarlemmerliede en Spaarnwoude*, *Haarlem, Bloemendal*). The *old configuration* of the *IJmuiden sea lock* was composed of a main canal that connected the North Sea with the city of Amsterdam through six sea locks, as indicated with yellow arrows in Fig. 2. Several strategic activities for the Dutch community take place nearby the *IJmuiden sea lock*: the storage and trans-shipment of fresh and deep-frozen fish, ferry and cruise shipping and assembly and construction of offshore wind farms. Small artificial hills hiding large shelters dating back to World War II and currently used to store frozen fish as well as sand dunes rise up along the North Sea coast. Cranes, offshore platforms, residential and industrial buildings surround the sea lock (Fig. 2).

In the Netherlands, about 26% of the land is placed in depressions and about 23.5% of the population lives below the mean sea level (Hut, 2015). The selected study area belongs to the so-called *"low-elevation coastal zones"* for which strong storms can give rise to dangerous conditions, infrastructural breakdown and other risks (McGranahan et al.,

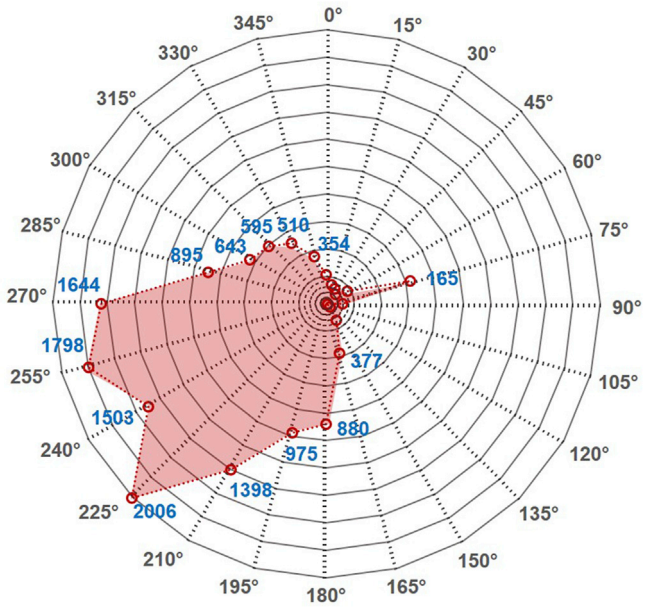

Fig. 6. Number of samples representing neutral or near-neutral atmospheric conditions collected in recording period July 5, 2017–July 5, 2018 for 24 reference wind directions.

2007). As illustrated in the map of Fig. 3a, about 91% has an altitude lower than 10 m above the mean sea level (MSL) and only about 9% has an altitude between 10 and 20 m MSL. These percentages do not include the area covered by buildings, bridges, cranes and other small obstacles (as artificial hills) concentrated around the *IJmuiden sea lock*. The sea lock area is comparable to an *open area* with a very low aerodynamic roughness and therefore exposed to strong wind conditions. Conversely, the area surrounding the sea lock exhibits a high presence of buildings of different heights (Fig. 3a), typically comparable to an *urban area*, therefore a high aerodynamic roughness. The combination of these two features makes this *seaport area* quite unique and highly exposed to complex wind conditions (such as separation and recirculation flows around buildings and ships) especially in case of strong sea storms.

Major changes to the *old configuration* of the *sea lock* were initiated starting January 2016 when a *new sea lock* started to be constructed (Fig. 3b–c). Because of the ongoing period of drought and the increasing ship sizes, and based on the advice of the National Water Coordination Committee, several actions were taken by the Directorate-General for Public Works and Water Management (Port of Amsterdam, 2018). One of these decisions was to adjust the lock passage regime in IJmuiden to reduce saltwater intrusion from the North Sea Canal into the Amsterdam Rhine Canal and accommodate larger cruise ships as well as container ships (Port of Amsterdam, 2018). The *new sea lock* should be operative by January 2022. In the *new configuration*, it is 500 m long, 70 m wide and 18 m deep and it will accommodate vessels of maximum 365 m in length, 57 m in width and 13.75 m in depth. It will be 100 m longer, 20 m wider and 3 m deeper than the old *Noordersluis* lock, which was one of the largest in the world in the year of its completion in 1929 (Fig. 3b–c). The *new sea lock* not only differs from the *Noordersluis* in terms of size, it will also have a wider range of use, because it is deeper than the old one and it can be operated regardless of the tides. Moreover, the lock walls will soar 5 m above the current water level providing defense against the rising sea levels caused by climate change and strengthening the country's flood control. A comparison among the *old* configuration (2015), the new configuration at the beginning of the construction (2017), and a recent status of construction of the new sea lock (2019) is shown in Fig. 4.

3. On-site measurements

On-site measurements of wind speed and wind direction were carried out with 2D ultrasonic anemometers at four positions, termed *IJm1*, *IJm2*, *IJm3* and *IJm4* (Fig. 5). Data were gathered with a sampling frequency of 1 Hz for a period of 12 months (from July 5, 2017 to July 5, 2018) with some minor interruptions in between due to storms and equipment malfunctioning. The anemometer stations were installed in the area of the sea lock at a height of about 15 m MSL (Fig. 5). The anemometer positions were chosen (*i*) to properly represent the wind conditions around the sea lock and (*ii*) to avoid as much as possible local disturbance effects caused by local small-scale terrain and building features that are not included in detail in the computational model. The station *IJm1* was

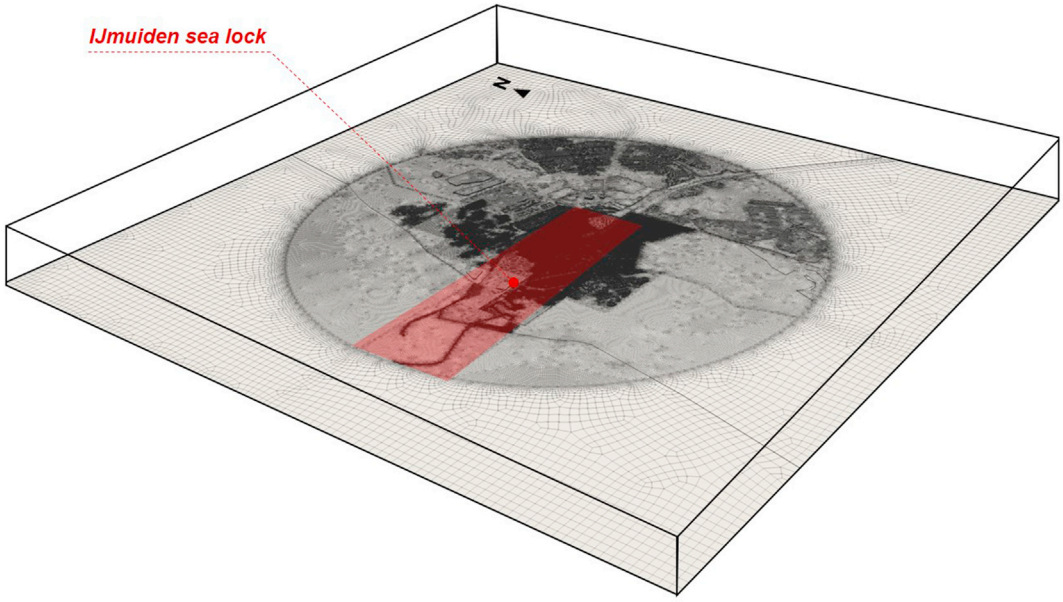

Fig. 7. Computational domain and grid on the bottom surfaces of the domain.

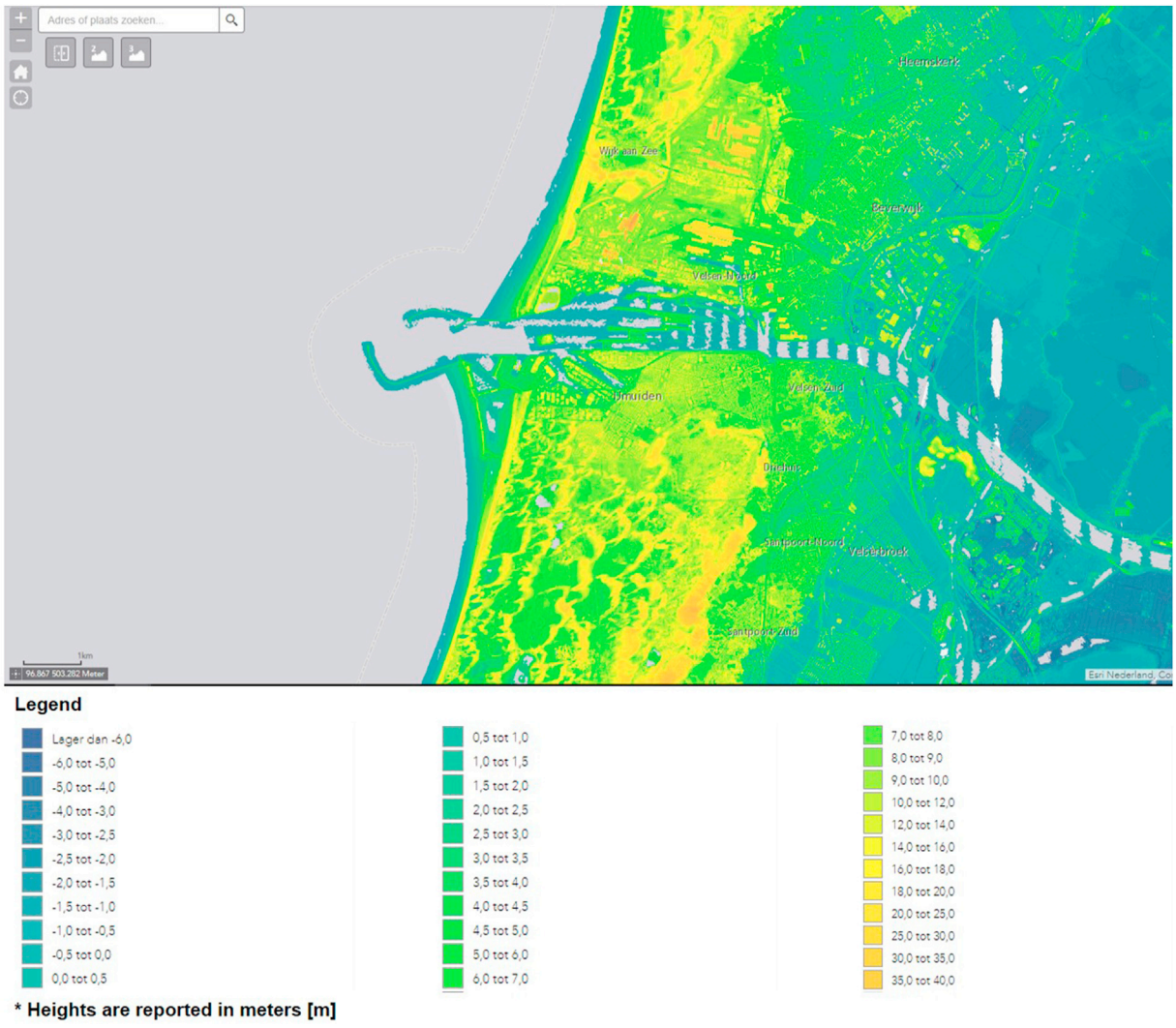

Fig. 8. Screenshot of the *"Actueel Hoogtebestand Nederland"* webpage showing the surface height (m) of the selected area for analysis. Legend enlarged for readability.

intentionally installed nearby the station *KNMI*, already in place for a long time and property of the KNMI (Royal Dutch Meteorological Institute). This KNMI station included more traditional measurement equipment, such as a cup anemometer and a wind vane. At this position, the measurements appeared to be not significantly influenced by the immediate surroundings (Fig. 5). This station will be essential for future operation where the measured conditions at this station will be translated to local wind speed and local wind direction at every location in the sea lock by means of the results of the CFD simulations presented in this paper. The position of *IJm1* was chosen as reference position and the measured mean wind speed at this location is denoted as U_{ref}.

For CFD validation, the on-site measurements of *IJm1*, *IJm2*, *IJm3* and *IJm4* were averaged into 10-min data. From the resulting database composed of 10-min mean wind speed (U) values, only those data likely associated with neutral atmospheric stratification conditions were retained (Stull, 1988). In accordance with the Pasquill (1961) and Venkatram (1996) stability classes and in absence of temperature data, only samples (i.e. the 10-min mean wind speed values) larger than 6 m/s were considered in the validation study. This was important to exclude thermal effects from the comparison. Around each wind direction ($\theta = 0°$, 15°, …, 345°) for which CFD simulations were performed, a relatively narrow 15° (i.e. ±7.5°) wind direction sector was defined. For every sector, all 10-min data values with mean 10-min wind directions at the reference station *IJm1* within this sector were grouped. The amplification factors (K_{exp}), defined as the ratio between U at the measurement position (e.g. at *IJm2*, *IJm3* and *IJm4*) and U_{ref}, were averaged and the standard deviation (σ) was calculated. Fig. 6 indicates the number of samples (i.e. 10-min mean wind speed values larger than 6 m/s) representative of neutral atmospheric conditions collected in the recording period (July 5, 2017–July 5, 2018) for each of the 24 wind direction sectors (θ). Fig. 6 clearly shows that the prevailing winds blow mainly from South-West and West in a range of about 60° (i.e. from 210° to 270°). Only a very limited number of samples satisfying the above-mentioned selection criteria were found for the South-East, East and North-East sectors, especially for $\theta = 105°$ and $\theta = 120°$ for which only 11 and 12 samples were collected, respectively.

4. CFD simulations

4.1. Computational geometry, domain and grid

A high-resolution computational geometry and grid with a surface area of 225 km^2 (i.e. L x L x $H = 15 \times 15 \times 0.5$ km^3) were built using the software Gambit 2.4.6 (Fluent Inc., 2005) (Fig. 7). The whole computational geometry was constructed based on the ground plan (i.e. CAD drawings) of the area provided by the *"Publieke Dienstverlening op de*

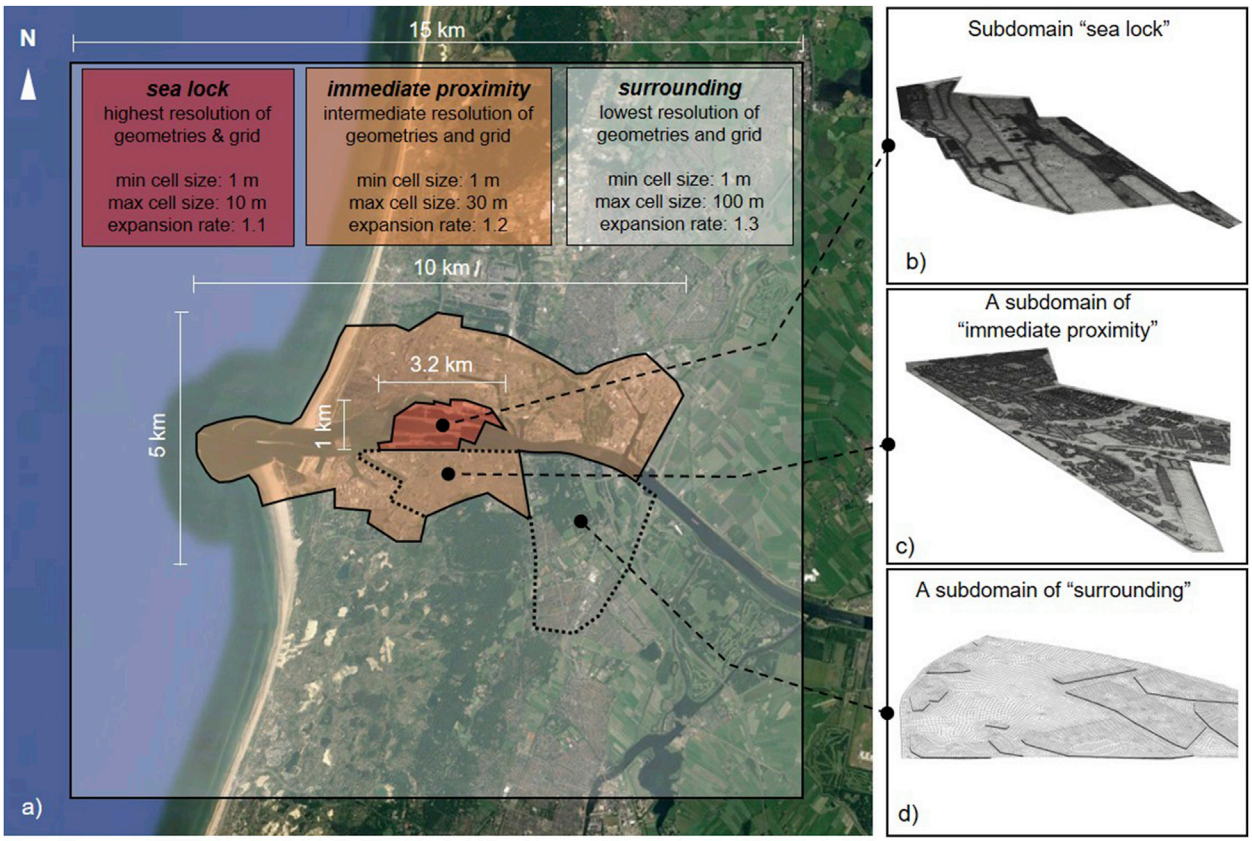

Fig. 9. Overview of the study area (*a*) inside the computational domain with an indication of three subdomains belonging to the three zones with different levels of geometrical detailing and grid resolution: (*b*) *"sea lock"*, (*c*) *"immediate proximity"*, (*d*) *"surrounding"*. Background photo credit to *Google Maps*.

Kaart" (Public Service of Maps of the Netherlands) combined with an accuracy check of each building using *Google Earth Pro* and *Google Maps*. However, since the *new configuration* of the *IJmuiden sea lock* was not included yet in these maps, 2D and 3D drawings provided by the harbor authority were used to construct the computational geometry. The height of each building, dock, crane and other permanent obstacles in the study area was obtained from the digital maps of Netherlands provided by *"Actueel Hoogtebestand Nederland"* (Fig. 8).

To construct a high-quality computational grid, the surface-grid extrusion technique presented by van Hooff and Blocken (2010) was used and the best practice guidelines for CFD in general and for CFD in wind engineering in particular were followed (Casey and Wintergerste, 2000; Britter and Shatzmann, 2007; Blocken and Gualtieri, 2012; Franke et al., 2007; Tominaga et al., 2008; Blocken 2015). To avoid potential convergence problems associated with the use of lower-quality grid cells when combined with the required second-order discretization schemes, only hexahedral and prismatic cells were used to construct the grid. As indicated in Fig. 9, three different levels of resolution were defined for both the geometry and grid (e.g. buildings, bridges and docks) for the computational domain with a stretching ratio ranging between 1.1 and 1.3, in adherence to the best practice guidelines (Franke et al., 2007; Tominaga et al., 2008). In zone 1, called *"sea lock"* and corresponding to the *new configuration* of the *IJmuiden sea lock* (Figs 8 and 9), the buildings, bridges and docks were constructed with their real ground plans and heights, but pitched roofs of buildings were represented by flat roofs and a minimum and a maximum cell size of 1 m and 10 m were used, respectively. Note that the effect of replacing pitched roofs with flat roofs on overall wind flow patterns was investigated earlier by Ricci et al. (2017; 2018) who noted negligible deviations in terms of mean wind speed between the *detailed* (including the real pitched roofs) and the *approximated* (simplifying pitched roofs by flat roofs) model inside the urban boundary layer (UBL). The computational grid of zone 1 counted about 27 million control volumes. In zone 2, termed *"immediate proximity"*, an intermediate level of resolution for the geometries and grid was applied (Fig. 9). In this zone of about 50.8 km^2, the buildings were also constructed with their real ground plans and heights and pitched roofs were replaced by flat ones, however a coarser grid was applied compared to zone 1. A minimum and a maximum cell size of 1 m and 30 m were adopted, respectively, yielding about 24 million control volumes for this zone. In the third zone, termed *"surrounding"* with about 167 km^2, a lower resolution for both geometry and grid was adopted compared to the foregoing two zones (Figs. 9 and 10). Due to the significant size of the computational domain, this further simplification was deemed necessary to reduce the overall computational costs. In this zone, groups of buildings were modeled as one block with a height equal to the average height of the buildings it represents. A minimum and a maximum cell size of 1 m and 100 m were adopted, respectively. This zone counted about 23 million control volumes. The whole computational grid counted approximately 74 million control volumes (Fig. 10).

4.2. Boundary conditions

A distinction between two types of roughness was made (Blocken 2015): (*i*) the surface roughness of terrains and obstacles (e.g. buildings, cranes, docks) that are explicitly included in the computational domain, i.e. with their actual shape and size (albeit possibly simplified) and (*ii*) the surface roughness of the surroundings (i.e. terrain and obstacles) that are not explicitly included in the computational domain. In both cases (*i* and *ii*) the aerodynamic roughness length (z_0) was determined in accordance with the Davenport roughness classification updated by

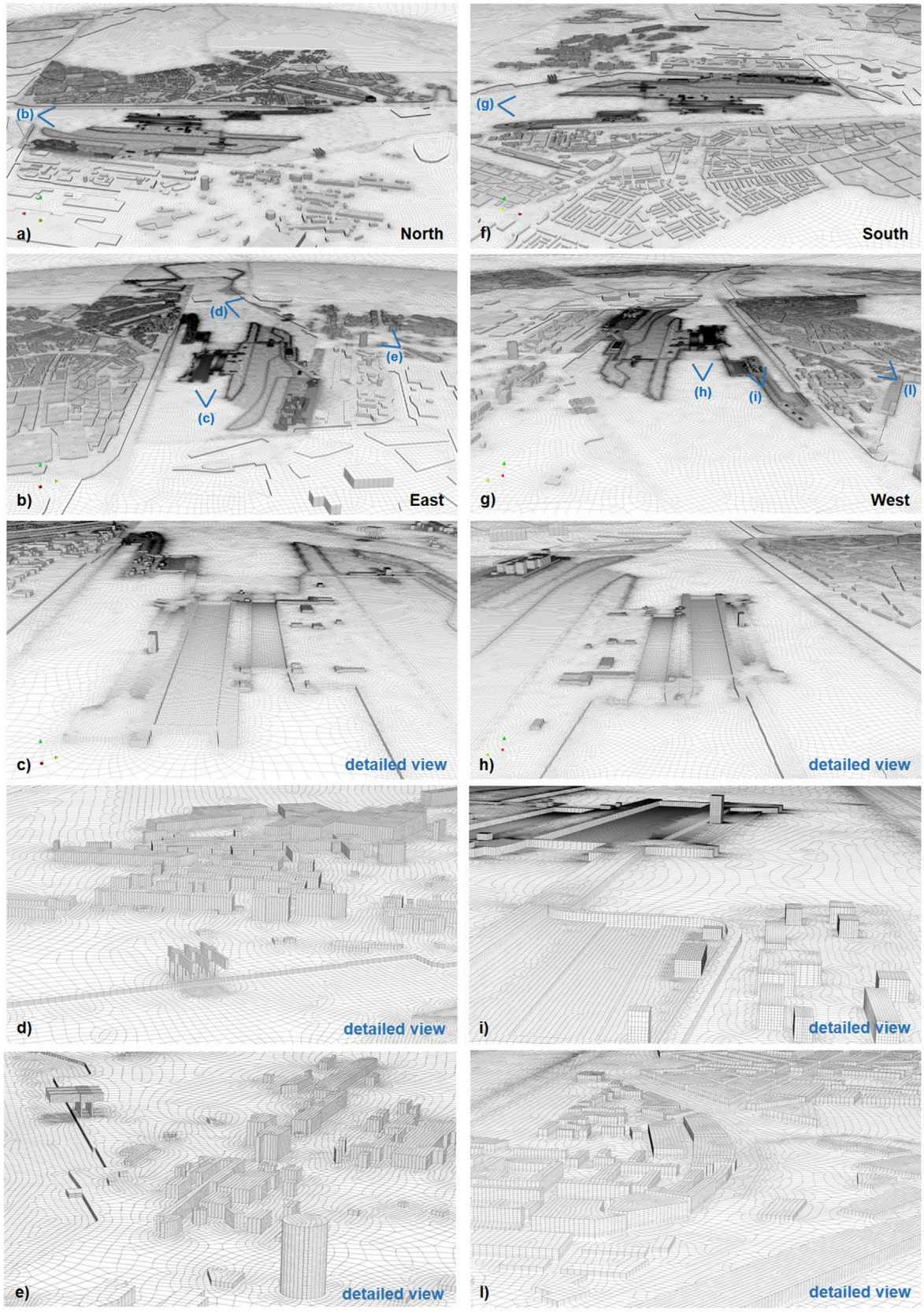

Fig. 10. Computational grid from different perspective views. Total cell count is 74 million.

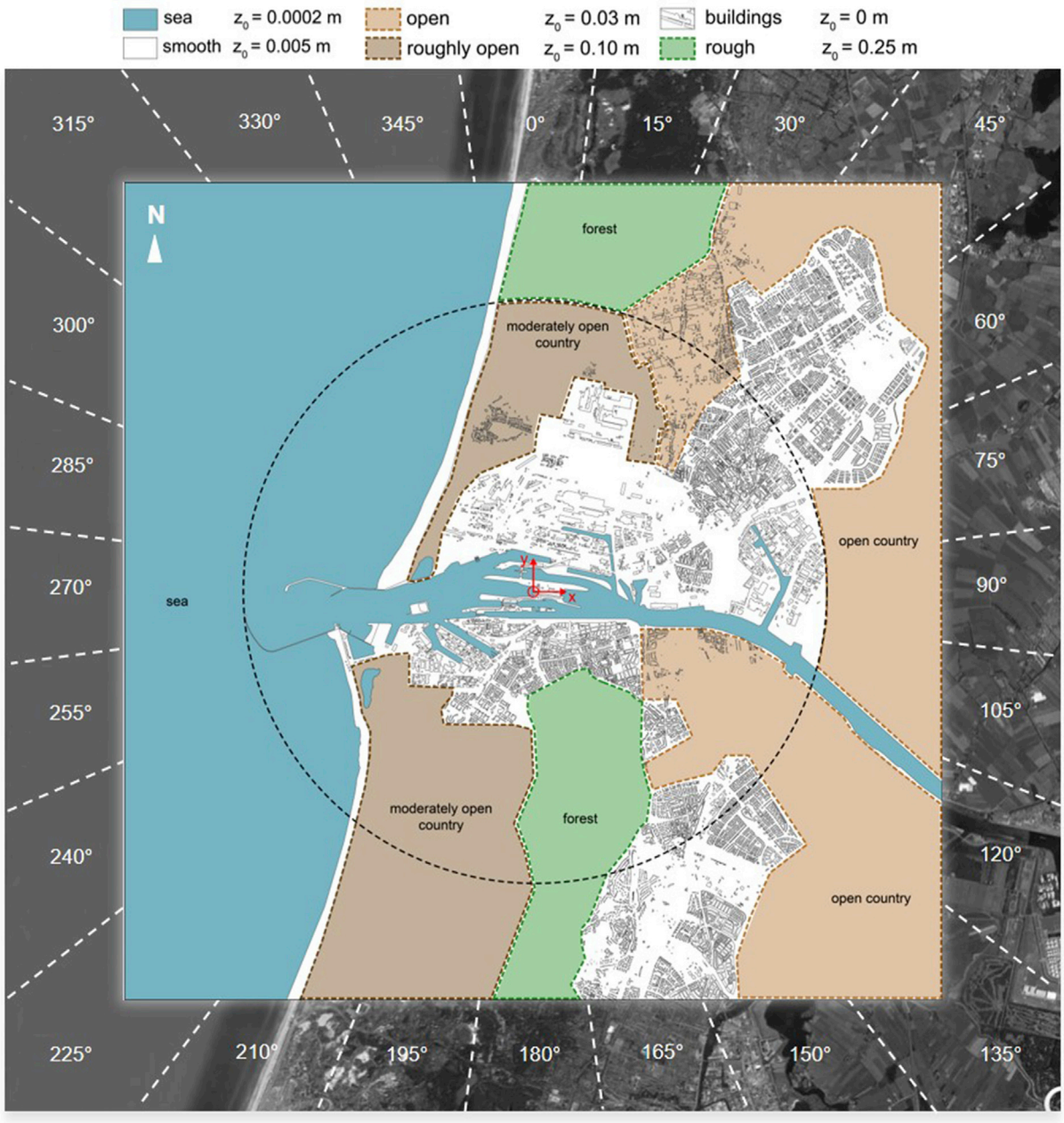

Fig. 11. Indication of the 24 wind sectors (i.e. reference wind directions) and the aerodynamic roughness lengths (z_0) for the terrain surrounding the study area. Background photo credit to *Google Maps*.

Wieringa (1992) and using *Google Maps*(Fig. 11). The surface roughness of the terrain outside the computational domain plays an important role since it determines to a large extent the shapes of the approach-flow profiles which in turn can affect the wind-flow pattern nearby the area under investigation (Ricci et al., 2019). The vertical profiles of mean wind speed (U); turbulence kinetic energy (k) and turbulence dissipation rate (ε) profiles were given by:

$$U = \frac{u_*}{\kappa} \, ln \frac{(z + z_0)}{z_0} \tag{1}$$

$$k = \frac{u_*^2}{\sqrt{C_\mu}} \tag{2}$$

$$\varepsilon = \frac{u_*^3}{\kappa(z + z_0)} \tag{3}$$

With u^* the friction velocity, z_0 the aerodynamic roughness length, κ the von Karman constant (equal to 0.41) and C_μ a constant (equal to 0.09). Fig. 12 shows the profiles for $z_0 = 0.0002$ m (termed *"sea profile"*) and $z_0 = 0.03$ m (termed *"land profile"*), with U_{ref} the reference wind speed at reference height $z_{ref} = 500$ m. In Fig. 12, λ represents a characteristic length scale which was taken equal to the height (H = 0.5 km) of the computational domain.

The computational domain was meticulously subdivided into patches of different aerodynamic roughness length (z_0) as indicated in Fig. 11 and Table 1. The values of z_0 were subsequently converted into the corresponding equivalent sand-grain roughness height (k_S) and a roughness

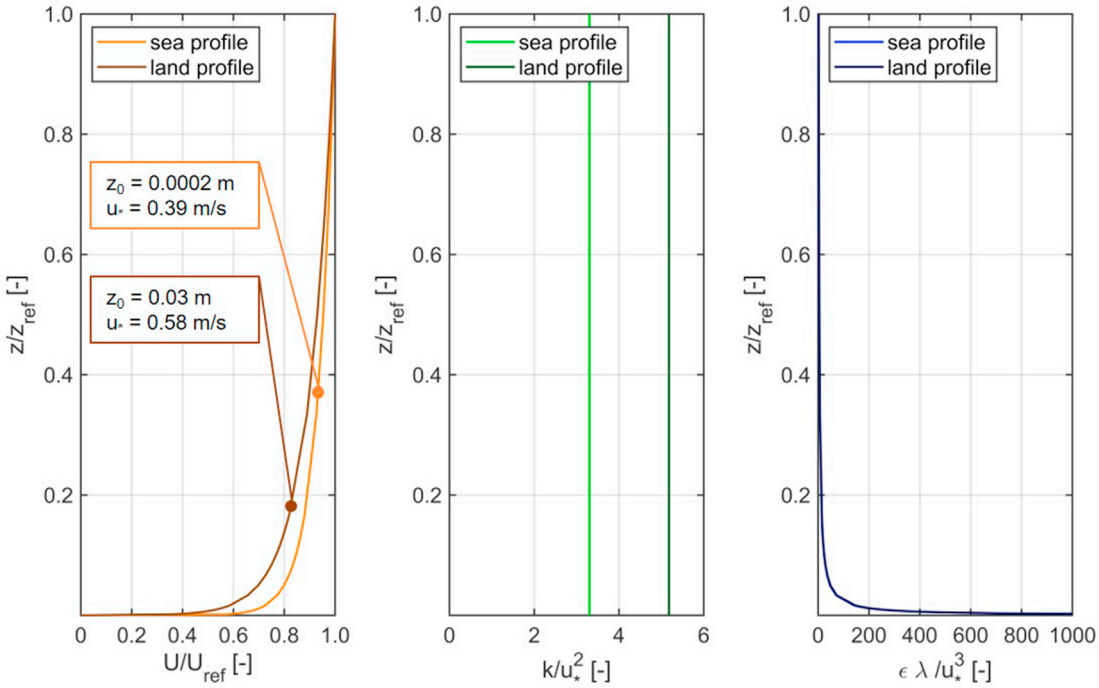

Fig. 12. Inflow conditions (U, k, ϵ) imposed at the inlet face of the computational domain for the reference wind directions $\theta = 270°$ (i.e. "*sea* profile") and $\theta = 0°$ (i.e. "land profile").

constant (C_S) in order to use the CFD code ANSYS Fluent 16 (ANSYS Fluent, 2013) in accordance with the equation by Blocken et al. (2007a, b) (Table 1):

$$k_s = \frac{9.793\, z_0}{C_s} \tag{4}$$

These values were required as input for the standard wall functions by Launder and Spalding (1974) with roughness modification by Cebeci and Bradshaw (1997).

At the sides (only for $\theta = 0°$, $\theta = 90°$, $\theta = 180°$ and $\theta = 270°$) and top of the computational domain a slip wall boundary condition was imposed. At the outlet, zero static gauge pressure was set.

4.3. Other computational settings

3D steady-state RANS CFD simulations were performed for 24 reference wind directions (θ) using the realizable k-ε turbulence model for closure (Shih et al., 1995). The choice for the realizable k-ε turbulence model was based on the accuracy and reliability proven by 3D steady RANS simulations carried out by other researchers on wind flows in complex areas, as van Hooff and Blocken (2010), Karava et al. (2011), Moonen et al. (2011), Janssen et al. (2013), Yang et al. (2016), Blocken et al. (2016), van Druenen et al. (2019), Antoniou et al. (2019). The second-order discretization schemes for the convective and the viscous terms of the governing equations and the SIMPLE algorithm for pressure-velocity coupling were adopted (Ferziger and Perić, 2002; Versteeg and Malalasekera, 2007). Each simulation was carried out by for approximately 144 h, using 16 cores of the cluster of the unit Building Physics & Services at the Department of the Built Environment of Eindhoven University of Technology. The simulations were terminated after about 45,000 iterations, when the scaled residuals had reached values of 10^{-5} for the continuity, 10^{-8} for x-, y- and z -velocity, 10^{-7} for k and 10^{-6} for ε.

5. CFD and on-site measurement results

5.1. Contours of wind speed amplification factor

Fig. 13 presents the CFD results as contours of the mean wind speed amplification factor (K) in a horizontal plane at about 15 m above MSL. As mentioned in Section 3, the station *IJm1* is taken as reference since at this location the wind flow field is supposed to be not significantly influenced by surrounding obstacles. Fig. 13 shows that in general, sheltering effects with separation and wake flow caused by the presence of obstacles such as buildings, cranes, docks and bridges and the changes in z_0 from patch to patch, are observed throughout the whole domain especially at the sea lock. These effects may be of great relevance for ships passing through the sea lock or just maneuvering nearby quays. In this regard, a qualitative representation of the wind flow experienced by a ship when passing the *IJmuiden sea lock* through the main route is also provided in Fig. 13 by means of a piece-wise linear trajectory from west to east. The line can be black or white, solid or dashed. The solid white line indicates a part of the trajectory with almost constant $K \leq 1$, the solid black line indicates a part with an almost constant $K > 1$ and the dashed black line indicates a part with strong gradients of K. Overall, the following observations are made:

Table 1
Aerodynamic roughness length (z_0), equivalent sand-grain roughness height (k_S) and roughness constant (C_S) values for surface roughness in the computational domain.

roughness patch	z_0 [m]	k_S [m]	C_S [-]
sea	0.0002	3.92×10^{-3}	0.5
smooth	0.005	9.79×10^{-2}	0.5
open	0.03	4.19×10^{-1}	0.7
roughly open	0.10	4.89×10^{-1}	2.0
rough	0.25	4.89×10^{-1}	5.0

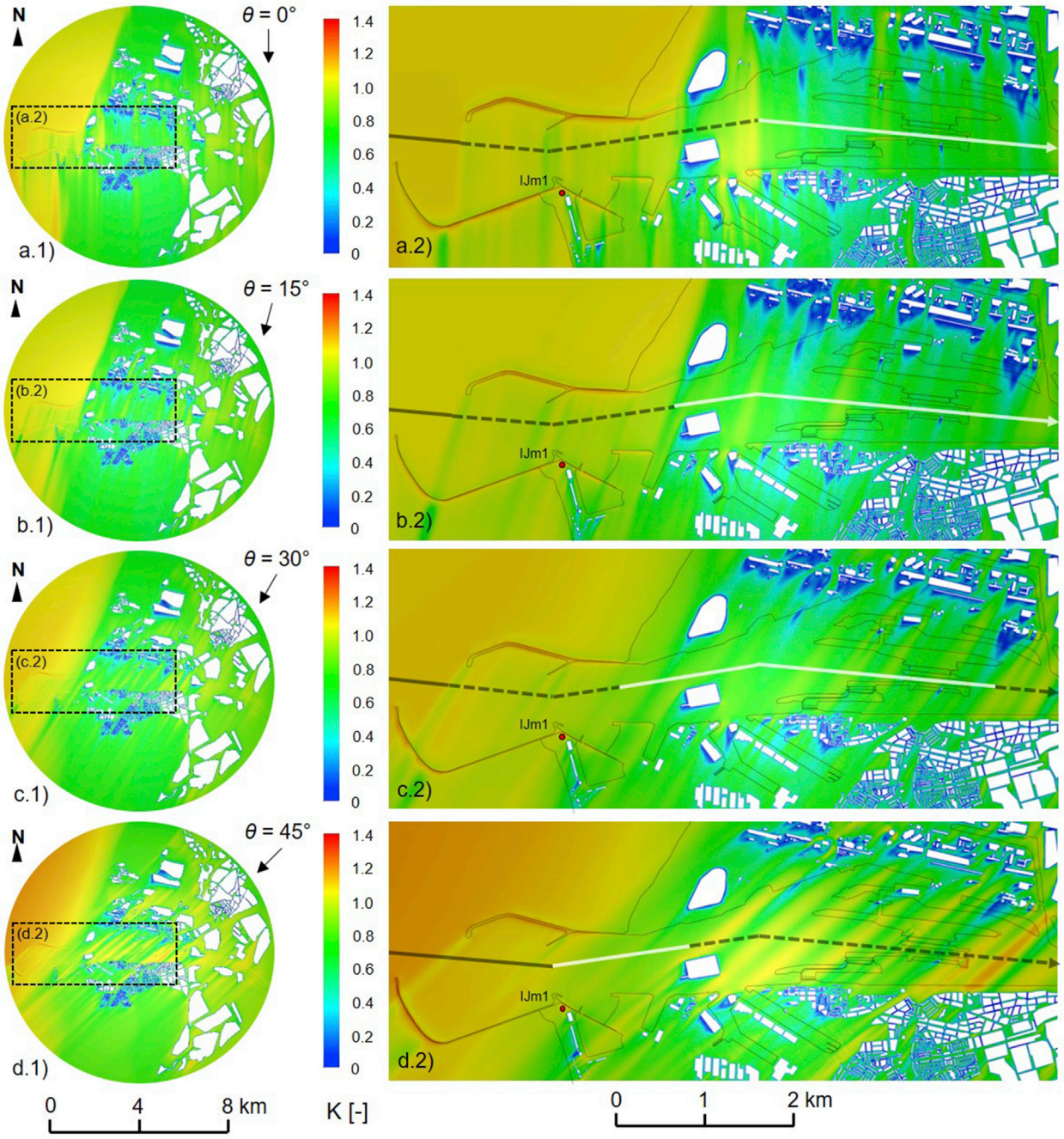

Fig. 13. **(a–d)** Contours of amplification factor (K) at 15 m above mean sea level (MSL), for the reference wind directions $\theta = 0°$, $\theta = 15°$, $\theta = 30°$ and $\theta = 45°$. The main ship's route in the sea lock is also indicated: a solid white line for an almost constant $K \leq 1$, a solid black line for an almost constant $K > 1$ and a dashed black line for strong gradients of K. **(e–h)** Contours of amplification factor (K) at 15 m above mean sea level (MSL), for the reference wind directions $\theta = 60°$, $\theta = 75°$, $\theta = 90°$ and $\theta = 105°$. The main ship's route in the sea lock is also indicated: a solid white line for an almost constant $K \leq 1$, a solid black line for an almost constant $K > 1$ and a dashed black line for strong gradients of K. **(i–n)** Contours of amplification factor (K) at 15 m above mean sea level (MSL), for the reference wind directions $\theta = 120°$, $\theta = 135°$, $\theta = 150°$ and $\theta = 165°$. The main ship's route in the sea lock is also indicated: a solid white line for an almost constant $K \leq 1$, a solid black line for an almost constant $K > 1$ and a dashed black line for strong gradients of K. **(o–r)** Contours of amplification factor (K) at 15 m above mean sea level (MSL), for the reference wind directions $\theta = 180°$, $\theta = 195°$, $\theta = 210°$ and $\theta = 225°$. The main ship's route in the sea lock is also indicated: a solid white line for an almost constant $K \leq 1$, a solid black line for an almost constant $K > 1$ and a dashed black line for strong gradients of K. **(s–v)** Contours of amplification factor (K) at 15 m above mean sea level (MSL), for the reference wind directions $\theta = 240°$, $\theta = 255°$, $\theta = 270°$ and $\theta = 285°$. The main ship's route in the sea lock is also indicated: a solid white line for an almost constant $K \leq 1$, a solid black line for an almost constant $K > 1$ and a dashed black line for strong gradients of K. **(w–z)** Contours of amplification factor (K) at 15 m above mean sea level (MSL), for the reference wind directions $\theta = 300°$, $\theta = 315°$, $\theta = 330°$ and $\theta = 345°$. The main ship's route in the sea lock is also indicated: a solid white line for an almost constant $K \leq 1$, a solid black line for an almost constant $K > 1$ and a dashed black line for strong gradients of K.

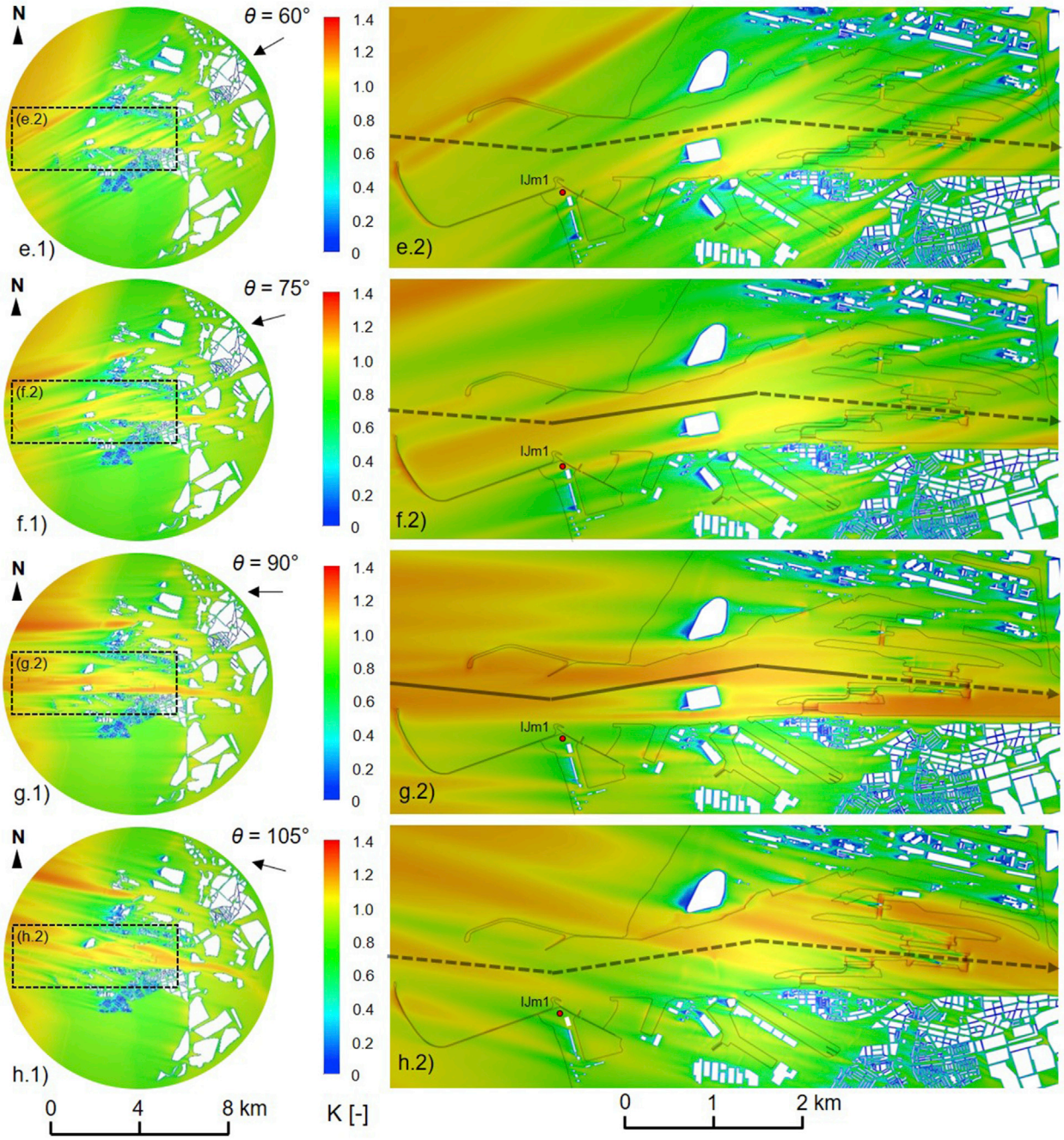

Fig. 13. (*continued*).

- For all θ a ship passing through the sea lock experiences strong wind speed gradients and due to the surrounding obstacles (e.g. buildings, cranes and quays). In particular a wide range of K, from 0.3 to 1.4, is observed in the sea lock for the wind sectors 45°–165° (Fig. 13d-n) and 240°–315° (Fig. 13s–v).
- There is generally an increase of K for all θ in the zones with a low z_0, as in the open sea and inside the sea lock (Figs. 3 and 13).
- A wider range of reduced K (i.e. green - blue range in the colorbar) versus increased K (i.e. orange - red range in the colorbar) is found especially at the urban area surrounding the sea lock for all θ (except for 0°, 15°, 30°, 330°) (Fig. 13).
- Large gradients of K are found for all θ in open areas (e.g. squares, parking and factories deposit areas) downstream of dense surroundings through which the flow is unable to funnel (Figs. 3 and 13).
- Small gradients of K are found for all θ in open areas (e.g. squares, parking and factories deposit areas) downstream of less dense surroundings through which the flow is able to funnel by narrow streets. (Fig. 13).
- Large gradients of K are found for East (i.e. $\theta = 75°$, $\theta = 90°$, $\theta = 105°$) and West (i.e. $\theta = 255°$, $\theta = 270°$, $\theta = 285°$) wind sectors of about 30°, when the main canal of the sea lock is almost aligned with the approach-flow direction. For these θ, the highest K are also observed along the main ship's route (Fig. 13f,g,h,t,u,v).

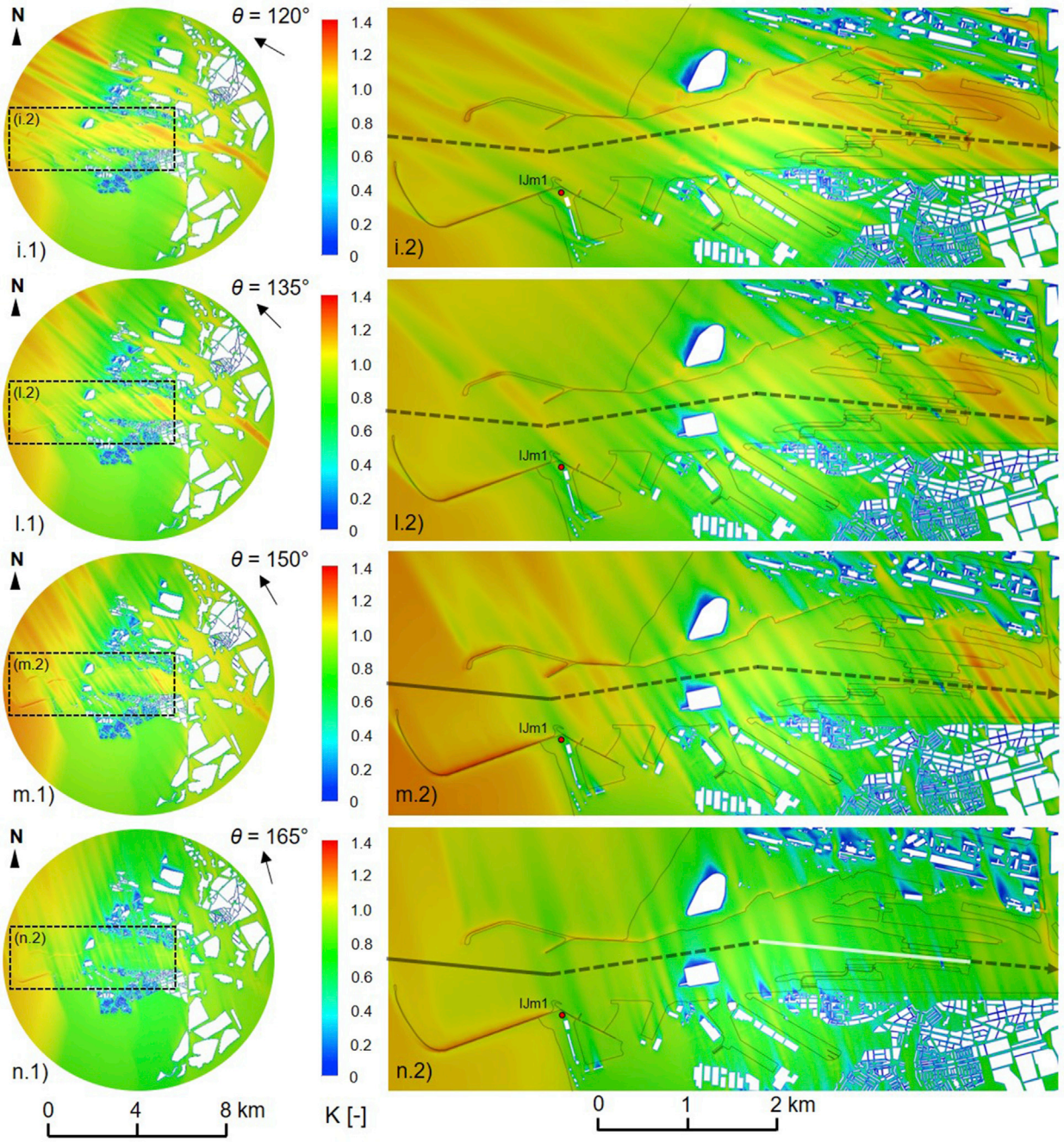

Fig. 13. (*continued*).

Fig. 13a–c shows that for $\theta = 0°$, $\theta = 15°$ and $\theta = 30°$ K varies from 0 to about 1.1, with higher factors (i.e. about 1.05 and 1.1) at open sea. However, this trend changes quite rapidly as soon as the presence of the buildings obstructs the winds blowing from East to West. Indeed, for $\theta = 45°$, $\theta = 60°$ and $\theta = 75°$ the contours of Fig. 13d–f shows large K (i.e. up to 1.4) at open areas as squares, parking and factories deposit areas. These effects become even larger in the wind sector 90°–165° reported in Fig. 13g-n. This can be attributed to the sheltered position of the station *IJm1* where lower wind speed values are observed compared to other wind sectors, as described in the next section. In the wind sector 180°–225°, the K values at the sea lock decrease slightly (about 0.8–1.0) and lower gradients are found inside the sea lock (Fig. 13o-s), with respect to the above-mentioned θ. Indeed, unlike the buildings belonging to the North-Eastern and Eastern *surrounding* zone (see Fig. 9), the buildings located to the South of the sea lock slightly obstruct the funneling of the flow. It happens because, as described in Section 4.1 by Fig. 9, in the *immediate proximity* of the sea lock each building was constructed with its real ground plan and height and the flow is able to funnel through the streets, squares and open areas.

In the wind sector 240°–300°, peak values of K (i.e. of about 1.28) are found at the sea and sea lock, where a low z_0 value (i.e. of 0.0002 m) was used (Fig. 13t-w). In this sector the *IJm1* station is slightly shielded by the structure of the quays. However, note that lower K values and smaller gradients, with respect to the analogous Eastern wind directions, are found throughout the whole computational domain due to the scarce presence of obstacles obstructing the wind flow funneling, between the

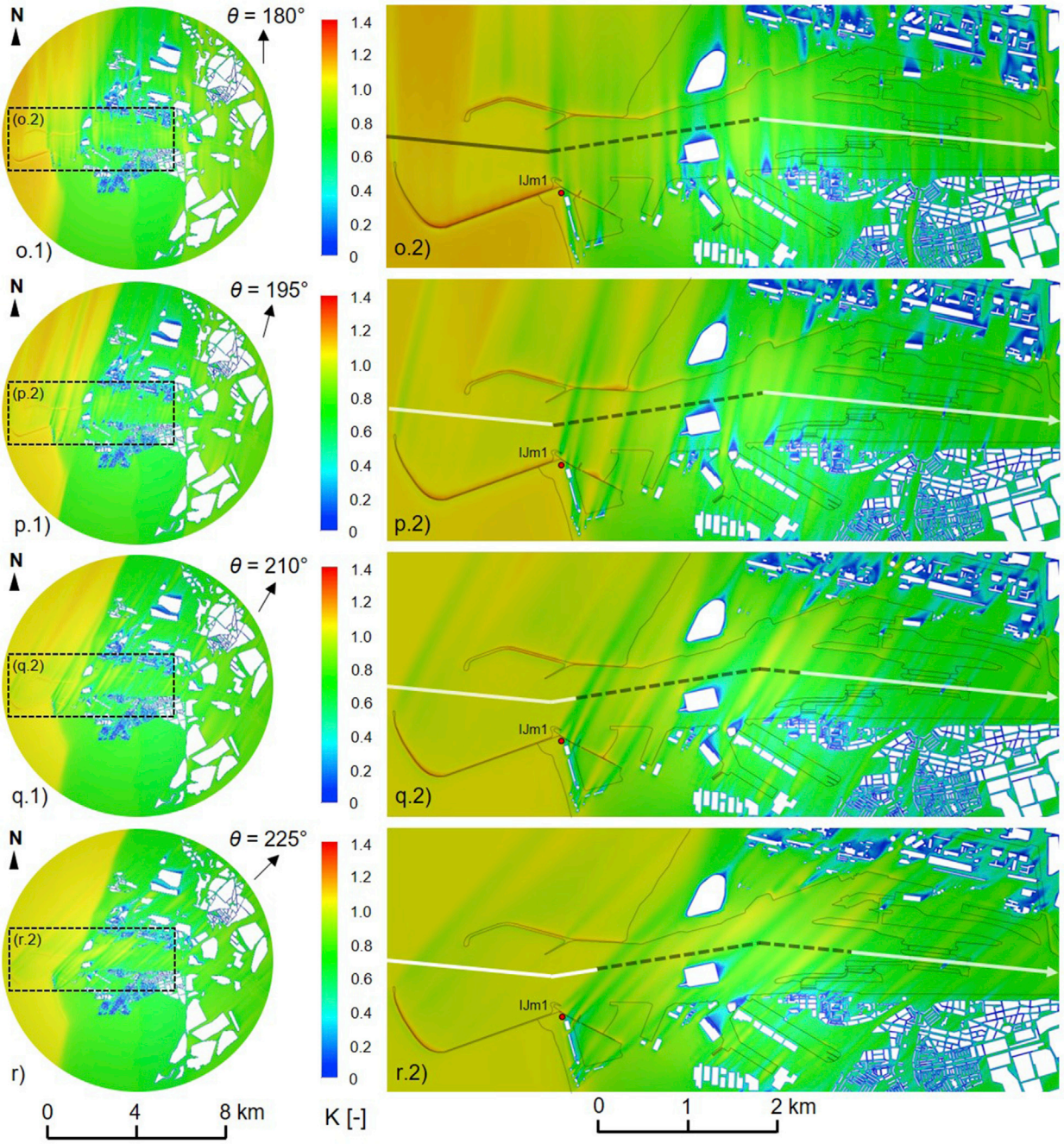

Fig. 13. (*continued*).

approaching flow and the sea lock (Fig. 13t-w).

In the wind sector 315°–345°, K varies between 0.7 and 1.1 at the sea lock (Fig. 13x-z). As already mentioned for the wind sector 180°–225°, the surrounding buildings (see Fig. 9) located to the North of the sea lock allow the wind-flow funnel preventing large separations of the flow zones mainly nearby the docks (Fig. 13 x,y,z).

Note that, as described in Section 4.1 (see also Fig. 9), in order to limit the total amount of cells, the computational grid in the *surrounding* zone generally has a lower resolution (than *sea lock* and *immediate proximity* zones). This can cause a less accurate wind flow prediction over, around, and between buildings in this zone, particularly for the wind sectors between 0° and 180°.

5.2. Comparison between simulated and measured data

This subsection presents a comparison between the CFD results and the on-site measurements in terms of wind speed amplification factor (K) and local wind direction (ϕ) for 24 reference wind directions (θ) at four measurement positions (i.e. *IJm1*, *IJm2*, *IJm3* and *IJm4*). The wind speed amplification factors of the measured, K_{exp}, and the simulated, K_{num}, data are defined analogously to those presented in the contours of Fig. 13. As an example, Figs. 14–17 illustrate contours of K in a horizontal plane at 15 m MSL with local inserts of the measured and simulated amplification factor vectors ($\vec{K}$) at four measurement positions (i.e. *IJm1*, *IJm2*, *IJm3* and *IJm4*) for four reference wind directions (i.e. $\theta = 45°$, 135°, 225° and 315°). The accompanying tables provide the mean values and standard

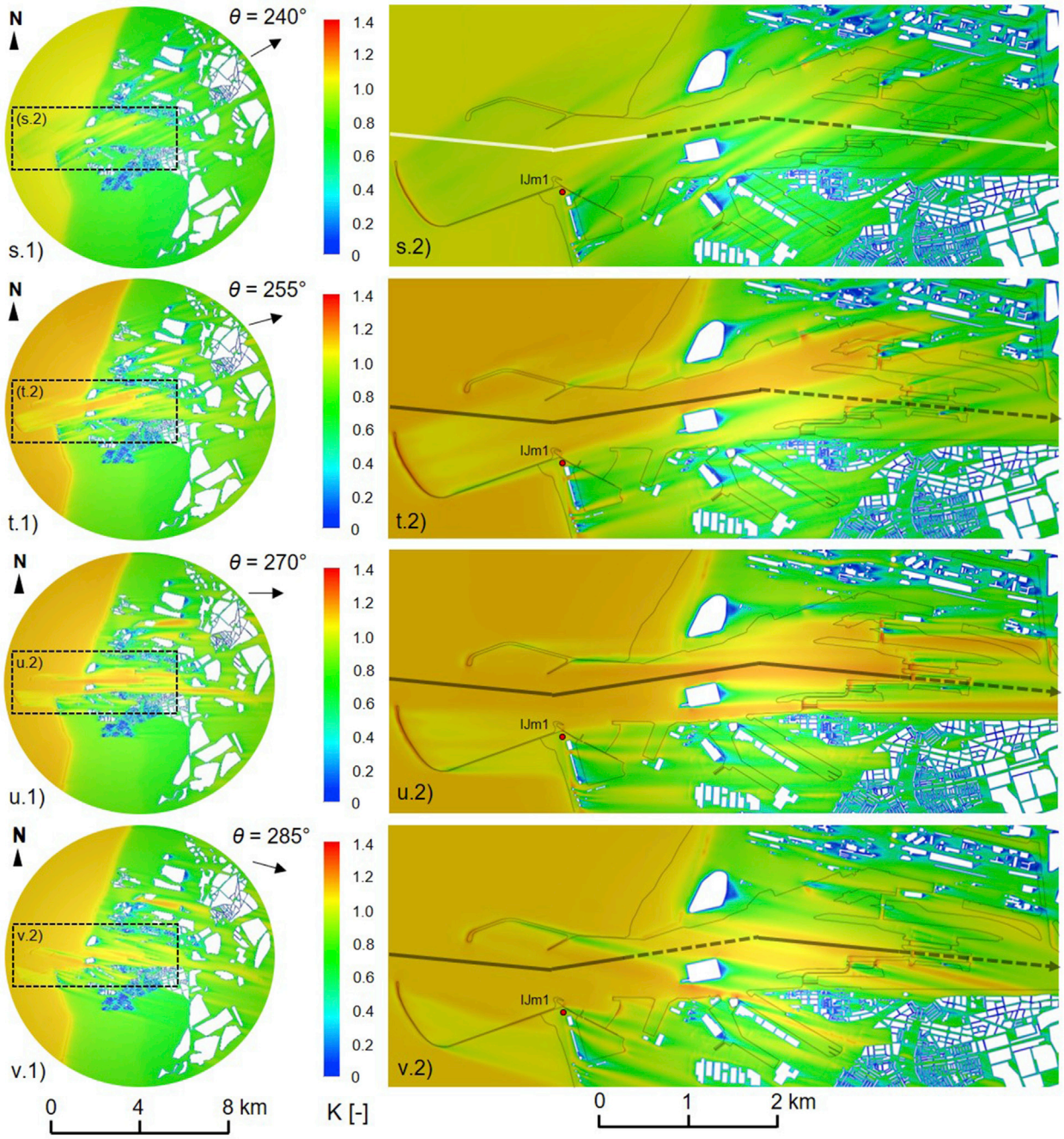

Fig. 13. (*continued*).

deviations of the measured data of $\vec{K}$ (K_{exp} - *avg.*, K_{exp} - *stdv.*) and ϕ (ϕ_{exp} - *avg.*, ϕ_{exp} - *stdv.*), as well as the values for the corresponding simulated data ($\vec{K}_{num}$) and (ϕ_{num}). Overall, the following observations are made:

- The wind flow inside the sea lock appears highly unsteady for all four wind sectors analyzed here, as indicated by the large values of ϕ_{exp} - *stdv* (e.g. max of 56.7) and K_{exp} - *stdv* (e.g. max of 0.23) at *IJm2*, *IJm3* and *IJm4*. Conversely, the ϕ_{exp} - *stdv* is found to be quite small (max of 4.4) at *IJm1* (Figs. 14–17) reconfirming this as a suitable reference position. Here, differences in terms of ϕ between simulated and measured data are small: 3.3° for $\theta = 45°$, to 1.5° for $\theta = 135°$, to 2.4° for $\theta = 225°$ and to 1.5° for $\theta = 315°$ (Figs. 14–17).
- For $\theta = 45°$ and $\theta = 135°$, despite the above-mentioned highly unsteady nature of the flow inside the sea lock, the difference between simulated and measured data in terms of $\vec{K}$ and φ varies in a range of 0.04–0.28 (at *IJm4* for $\theta = 45°$ and at *IJm3* for $\theta = 135°$) and 0°–35.9° (at *IJm3* and *IJm4* for $\theta = 135°$), respectively. At all stations, the predicted φ_{num} falls within the ϕ_{exp} - *stdv* (Figs. 14–17).
- For $\theta = 225°$ and $\theta = 315°$, the eastern part of the sea lock is less exposed to strong gradient of K due to the presence of the high-density surroundings through which the wind is not able to funnel. The difference between simulated and measured data in terms of $\vec{K}$ and ϕ varies in a range of 0.02–0.28 (at *IJm4* both for $\theta = 225°$ and $\theta = 315°$) and 2.1°–34° (at *IJm2* for $\theta = 225°$ and *IJm4* for $\theta = 315°$),

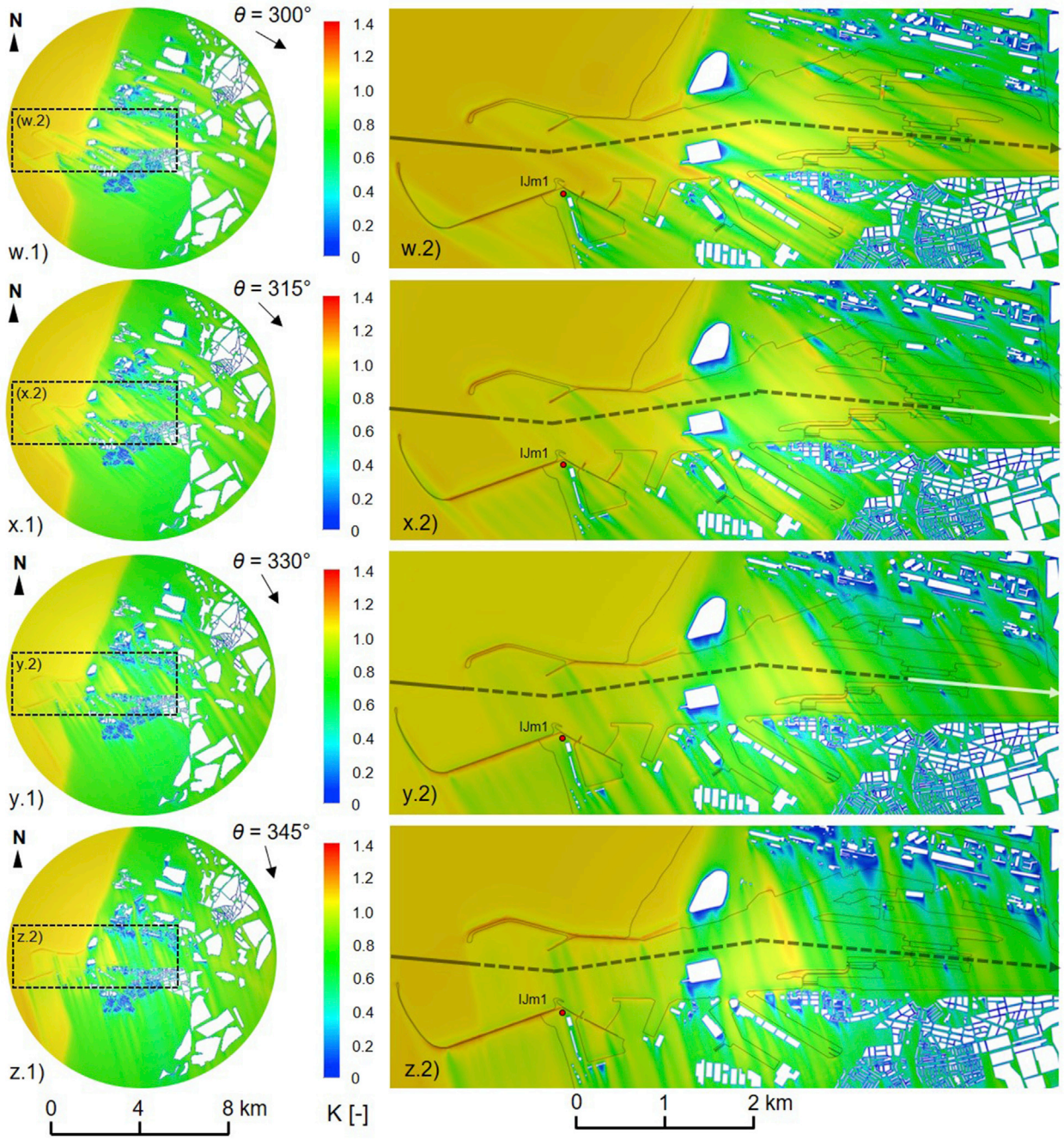

Fig. 13. (*continued*).

respectively. Also for these θ, at all stations the predicted ϕ_{num} falls within the ϕ_{exp} – *stdv* (Figs. 14–17).

Despite the high unsteadiness of the flow inside the sea lock mainly caused by the surrounding obstacles (as described in Section 5.1), the 3D steady RANS approach shows a sufficiently high reliability for predicting the mean wind speed and local wind direction. However, the deviations discussed in the present subsection and more in detail in the next one can be also caused by the fact that the comparison, between simulated and measured data, is carried out for two somewhat different sea lock configurations, being the *old* versus the *new* configuration.

5.3. CFD validation

Fig. 18 compare the measured and simulated wind speed amplification factor (K_{exp} and K_{num}), local wind direction (ϕ_{exp} and ϕ_{num}) and turbulence intensity amplification factor (Y_{exp} and Y_{num}), for the 24 reference wind directions at four positions (*IJm1*, *IJm2*, *IJm3* and *IJm4*). The latter is defined as the ratio between I at the measurement position (e.g. at *IJm2*, *IJm3* and *IJm4*) and I_{ref} at the reference position *IJm1*.

Fig. 18a shows a satisfactory agreement in terms of K between measured and simulated data with about 90% of the simulated data within ±30% deviation from the measured data, on a database of 72 samples. Deviations larger than 30% are found only for $\theta = 105°$ (at *IJm3*, *IJm3* and *IJm4*), $\theta = 120°$, $\theta = 330°$ (at *IJm4*) and $\theta = 345°$ (at *IJm3*).

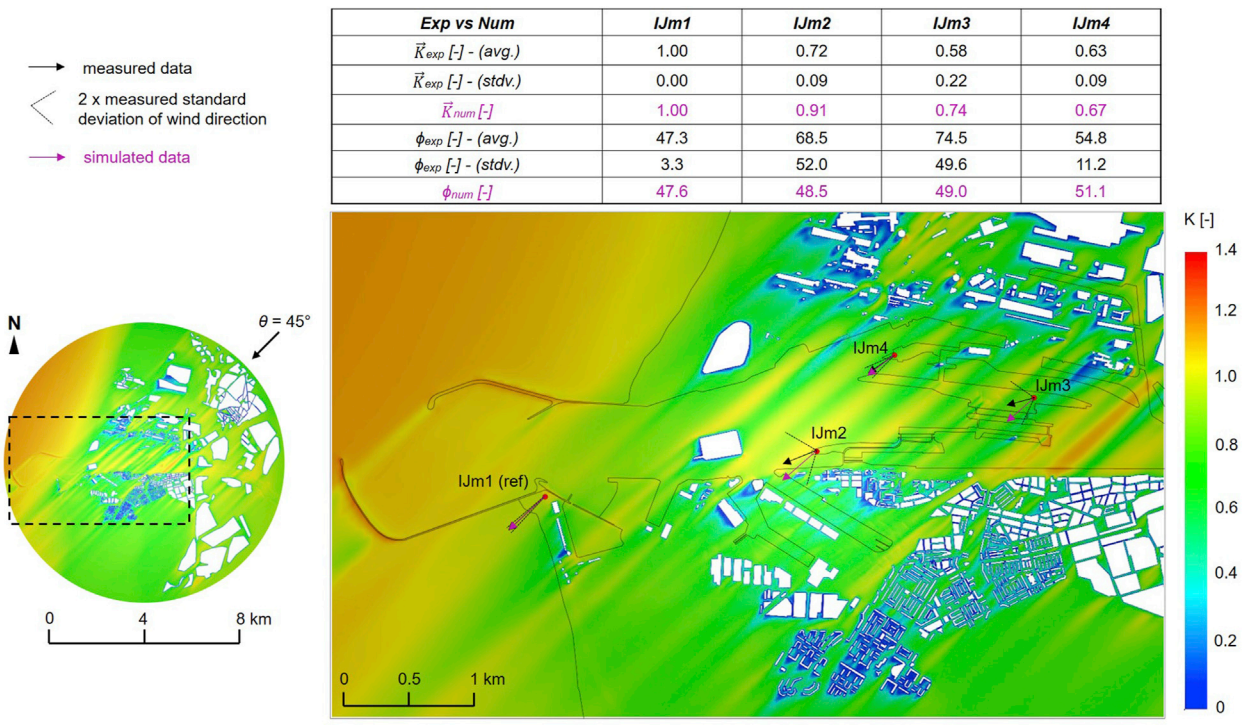

Exp vs Num	IJm1	IJm2	IJm3	IJm4
$\vec{K}_{exp}$ [-] - (avg.)	1.00	0.72	0.58	0.63
$\vec{K}_{exp}$ [-] - (stdv.)	0.00	0.09	0.22	0.09
$\vec{K}_{num}$ [-]	1.00	0.91	0.74	0.67
ϕ_{exp} [-] - (avg.)	47.3	68.5	74.5	54.8
ϕ_{exp} [-] - (stdv.)	3.3	52.0	49.6	11.2
ϕ_{num} [-]	47.6	48.5	49.0	51.1

Fig. 14. Contours of amplification factor (K) in a horizontal plane at 15 m above mean sea level (MSL) for the reference wind direction $\theta = 45°$. Wind speed ratio vectors ($\vec{K}$) at measurement positions *IJm1*, *IJm2*, *IJm3* and *IJm4*: simulated (violet) versus measured (black), with standard deviation (black). Average values and standard deviations of $\vec{K}$ and local wind direction (ϕ) are reported in the table. (For interpretation of the references to color in this figure legend, the reader is referred to the Web version of this article.)

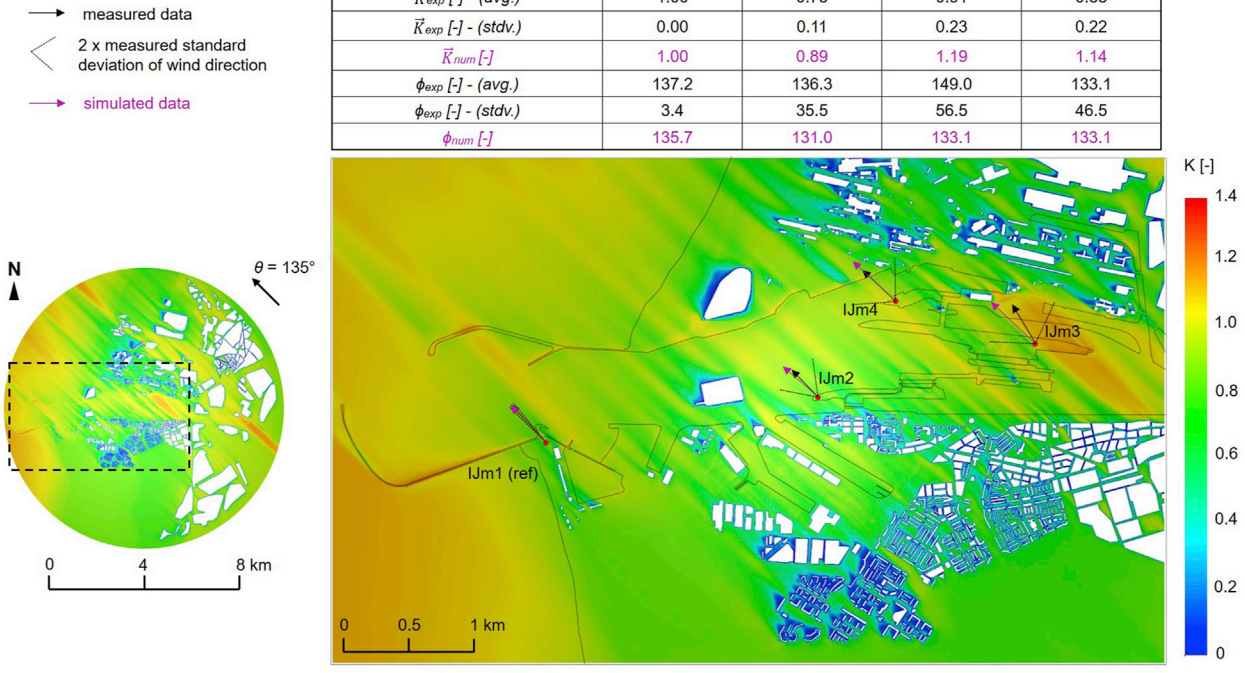

Exp vs Num	IJm1	IJm2	IJm3	IJm4
$\vec{K}_{exp}$ [-] - (avg.)	1.00	0.75	0.91	0.88
$\vec{K}_{exp}$ [-] - (stdv.)	0.00	0.11	0.23	0.22
$\vec{K}_{num}$ [-]	1.00	0.89	1.19	1.14
ϕ_{exp} [-] - (avg.)	137.2	136.3	149.0	133.1
ϕ_{exp} [-] - (stdv.)	3.4	35.5	56.5	46.5
ϕ_{num} [-]	135.7	131.0	133.1	133.1

Fig. 15. Contours of amplification factor (K) in a horizontal plane at 15 m above mean sea level (MSL) for the reference wind direction $\theta = 135°$. Wind speed ratio vectors ($\vec{K}$) at measurement positions *IJm1*, *IJm2*, *IJm3* and *IJm4*: simulated (violet) versus measured (black), with standard deviation (black). Average values and standard deviations of $\vec{K}$ and local wind direction (ϕ) are reported in the table. (For interpretation of the references to color in this figure legend, the reader is referred to the Web version of this article.)

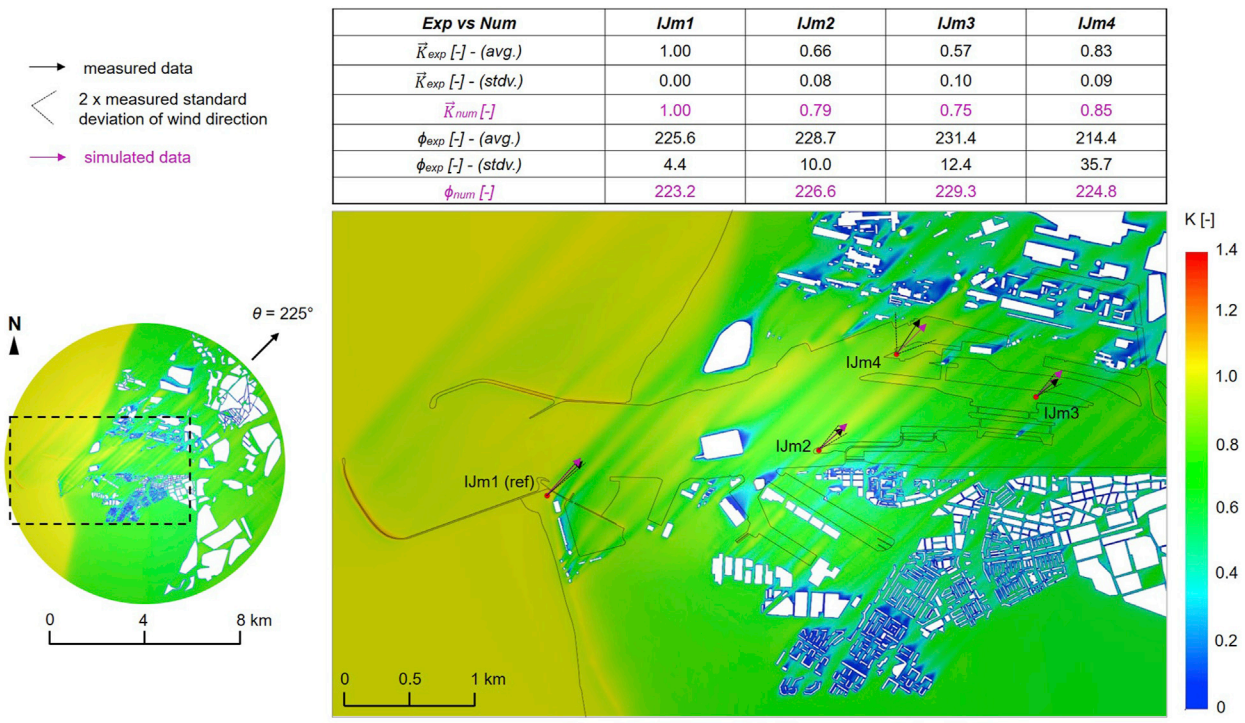

Exp vs Num	IJm1	IJm2	IJm3	IJm4
$\vec{K}_{exp}$ [-] - (avg.)	1.00	0.66	0.57	0.83
$\vec{K}_{exp}$ [-] - (stdv.)	0.00	0.08	0.10	0.09
$\vec{K}_{num}$ [-]	1.00	0.79	0.75	0.85
ϕ_{exp} [-] - (avg.)	225.6	228.7	231.4	214.4
ϕ_{exp} [-] - (stdv.)	4.4	10.0	12.4	35.7
ϕ_{num} [-]	223.2	226.6	229.3	224.8

Fig. 16. Contours of amplification factor (K) in a horizontal plane at 15 m above mean sea level (MSL) for the reference wind direction $\theta = 225°$. Wind speed ratio vectors ($\vec{K}$) at measurement positions *IJm1*, *IJm2*, *IJm3* and *IJm4*: simulated (violet) versus measured (black), with standard deviation (black). Average values and standard deviations of $\vec{K}$ and local wind direction (ϕ) are reported in the table. (For interpretation of the references to color in this figure legend, the reader is referred to the Web version of this article.)

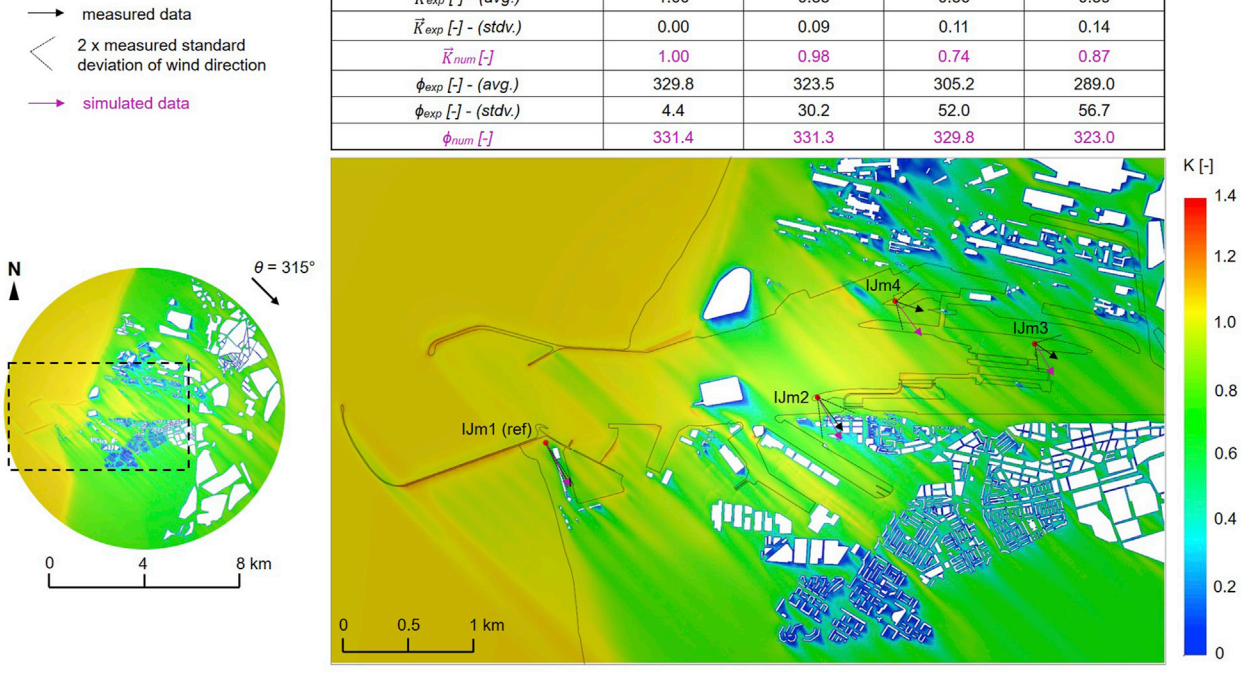

Exp vs Num	IJm1	IJm2	IJm3	IJm4
$\vec{K}_{exp}$ [-] - (avg.)	1.00	0.83	0.56	0.59
$\vec{K}_{exp}$ [-] - (stdv.)	0.00	0.09	0.11	0.14
$\vec{K}_{num}$ [-]	1.00	0.98	0.74	0.87
ϕ_{exp} [-] - (avg.)	329.8	323.5	305.2	289.0
ϕ_{exp} [-] - (stdv.)	4.4	30.2	52.0	56.7
ϕ_{num} [-]	331.4	331.3	329.8	323.0

Fig. 17. Contours of amplification factor (K) in a horizontal plane at 15 m above mean sea level (MSL) for the reference wind direction $\theta = 315°$. Wind speed ratio vectors ($\vec{K}$) at measurement positions *IJm1*, *IJm2*, *IJm3* and *IJm4*: simulated (violet) versus measured (black), with standard deviation (black). Average values and standard deviations of $\vec{K}$ and local wind direction (ϕ) are reported in the table. (For interpretation of the references to color in this figure legend, the reader is referred to the Web version of this article.)

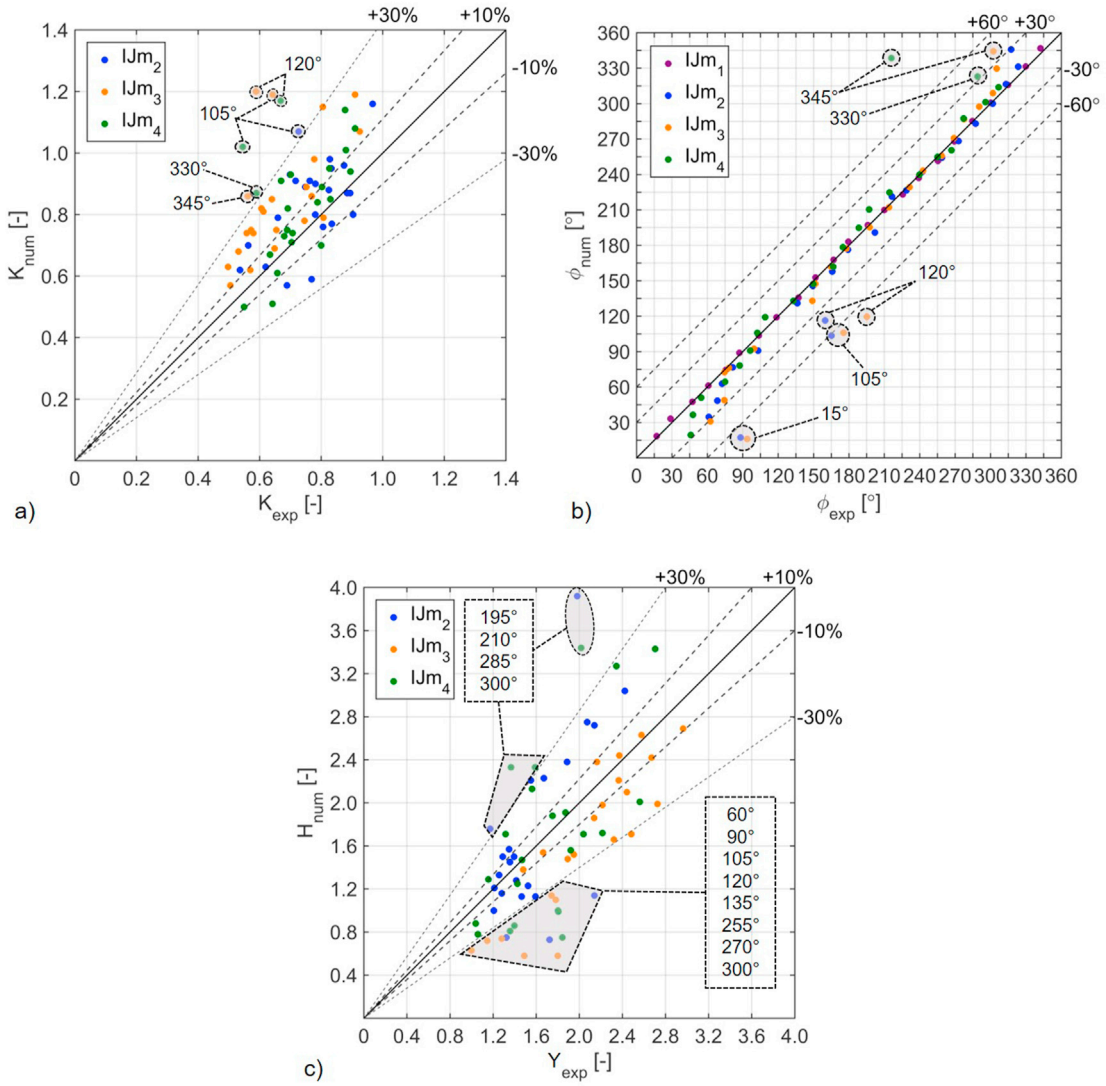

Fig. 18. Comparison between simulated and measured data at 15 m above mean sea level (MSL) at three measurement positions (*IJm2*, *IJm3* and *IJm4*) for 24 reference wind directions (θ): (*a*) wind speed amplification factor (K), (*b*) local wind directions (ϕ), (*c*) and turbulence intensity amplification factor (Y). Values of K, ϕ and Y with deviations between CFD and experiments exceeding 30%, 30° and 60° are also indicated in the figures.

To analyze the deviations larger than 30% at the four θ, polar diagrams are provided for *IJm2*, *IJm3* and *IJm4* (Fig. 19). At these positions, large deviations between K_{num} and K_{exp} are found mostly for the South-East - North-West wind sectors. In contrast, at *IJm2* and *IJm4* K_{num} are found to yield underestimations for 0°, 15°, 210°, 285°. However, since K is a ratio between a numerator (the value at *IJm2*, *IJm3* or *IJm4*) and a denominator (the value at the reference position, *IJm1*), the cause of such large deviations of K for 105°, 120°, 330°, 345° could be attributed to either deviations in the numerator or deviations in the denominator, or both. In this regard, the annual (July 2017–July 2018) average wind speed (of the selected 10-min mean wind speed values) of on-site measurements and the mean wind speed values of the 3D steady RANS simulations are compared by polar diagrams (Fig. 20) at *IJm1*, *IJm2*, *IJm3* and *IJm4*. The following observations are made:

- Deviations of 0.6%–8.4%, between simulated and measured data, are found at *IJm1* expect for three wind sectors (about 45°–135°, 240°–270°, 345°–45°), for which some over and underestimations are present. In particular, large underestimations (i.e. deviations of about 33%) by simulated data are found for $\theta = 105°$ and $\theta = 120°$ (Fig. 20).
- The deviations of K observed in Fig. 18a for $\theta = 105°$ and $\theta = 120°$ at *IJm3* and *IJm4* considerably exceed the 30% threshold. This is attributed to the fact that at positions *IJm3* and *IJm4,* the simulated U largely overestimates the measured U (i.e. deviations of about 55% for both θ) and the fact that at *IJm1* the simulated U underestimates the measured U with deviations of about 19.8% and 16.4%, respectively (Fig. 20a,c,d). This trend (overestimated data/underestimated data) between *local station* and *reference station* does not happen for other wind sectors (at least not to such an extent) but only for this wind sector ($\theta = 105°$ and $\theta = 120°$), for which the station *IJm1* is shielded by a small hill (with a height of about 5–7 m) not reproduced by the computational domain.
- Indeed the deviations of K, between simulated and measured data, observed in Fig. 18a for $\theta = 330°$ (at *IJm4*) $\theta = 345°$ (at *IJm3*) exceed the 30% threshold, because as shown by Fig. 20a,c,d the deviations between simulated U and measured U at *IJm4* and *IJm3* (i.e.

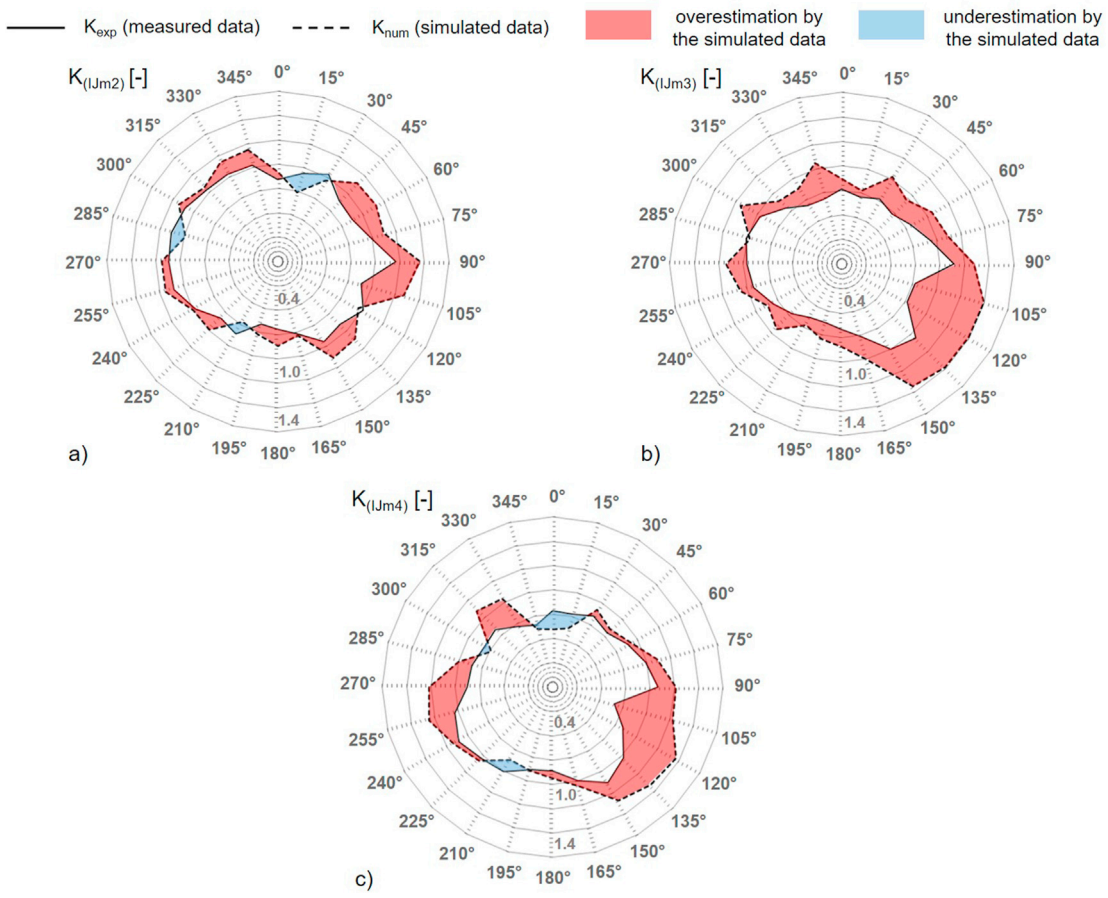

Fig. 19. Polar diagrams of measured (K_{exp}) and simulated (K_{num}) data in terms of wind speed amplification factors (K) calculated at three positions (*IJm1*, *IJm2* and *IJm4*) with *IJm1* as reference position and for 24 reference wind directions (θ).

deviations of about 60%) are larger than those at *IJm1* (i.e. deviations of about 8%).

- Finally, the deviations between simulated and measured data observed for $\theta = 105°$ at *IJm2* (Fig. 18a) could be attributed to the overestimation (i.e. deviation of about 21%) by simulated *U* found at *IJm2* and the underestimation (i.e. deviation of about 20%) by simulated *U* at *IJm1* (Fig. 20a–b).

Fig. 18b also shows a satisfactory agreement between measured and simulated data in terms of ϕ. A tight distribution around the diagonal is observed with about 90% of ϕ_{num} within ±30° of deviation with respect to ϕ_{exp}, on a database of 96 samples (i.e. 24 for each position). Deviations larger than 30%, between ϕ_{exp} and ϕ_{num}, are found for $\theta = 15°$ (at *IJm2* and *IJm3*), $\theta = 105°$ (at *IJm2* and *IJm3*), $\theta = 120°$ (at *IJm2* and *IJm3*), $\theta = 330°$ (at *IJm3* and *IJm4*) and $\theta = 345°$ (at *IJm4*). These results are further confirmed by Fig. 21, where the comparison between ϕ_{exp} and ϕ_{num} is displayed by polar diagrams at the four positions. At *IJm1* the agreement between ϕ_{exp} and ϕ_{num} is found to be almost perfect with small deviations of about 5°, not visible in the plot (Fig. 21a), in line with the contours of Figs. 14–17. At *IJm2*, ϕ_{num} underestimates ϕ_{exp} in the wind sector 15°–120°, with three peak values at $\theta = 15°$, $\theta = 105°$ and $\theta = 120°$ (Fig. 21b). In contrast, ϕ_{num} yields overestimations in the range 330°–345° (Fig. 21b). At *IJm3*, similar underestimations and overestimations by ϕ_{num} are found for 15°–120° and 315°–345°, respectively (Fig. 21c). At *IJm4*, the agreement between ϕ_{num} and ϕ_{exp} is observed to be very close for all wind sectors except 315°–345° (Fig. 21d).

As shown in Fig. 18c, less satisfactory agreement is noticed in terms of *Y*, which however is unsurprising given the use of the 3D steady RANS approach. A considerable scatter away from the diagonal is observed with - about 74% of Y_{num} (i.e. 53 samples) within ±30° with respect to the Y_{exp}, on a database of 72 samples. More insight can be obtained by the polar diagrams of Fig. 22. At *IJm2*, Y_{num} overestimates (with respect to Y_{exp}) are found for more than 50% of the wind sectors analyzed with a high peak value (equal to 3.97) at $\theta = 210°$ (Fig. 22a). For $\theta = 210°$, the *IJm2* station is shielded by a surrounding building (see Figs. 5 and 13q) and the inaccuracy of the steady RANS approach in predicting the wake flow can cause an underestimation (i.e. deviation of about 19%) by the simulated data in terms of mean wind speed (see also Fig. 20b) and an overestimation by the simulated data in terms of turbulence intensity. Conversely, at *IJm2*, Y_{num} yields underestimations for the sectors 330°–345° and 45°–120° (Fig. 22a). This position is shielded by the surrounding buildings (see also Fig. 5) and the RANS approach is found again to be less accurate since the Y_{num} underestimates Y_{exp} for almost all wind sectors (Fig. 22b). Finally, at *IJm4* underestimations interspersed with overestimations by Y_{num} are observed throughout the whole wind rose (Fig. 22c).

6. Summary and conclusions

Coastal areas and seaport areas are exposed to high wind speeds. These areas are generally characterized by a wide range of aerodynamic roughness lengths (e.g. sea versus densely built-up harbor docks) but also by numerous strong changes in surface roughness (e.g. from harbor basins to adjacent docks with container stacks and back to harbor basins, and so on). This combination makes the seaport area quite unique and exposed to highly complex wind conditions. A large number of activities

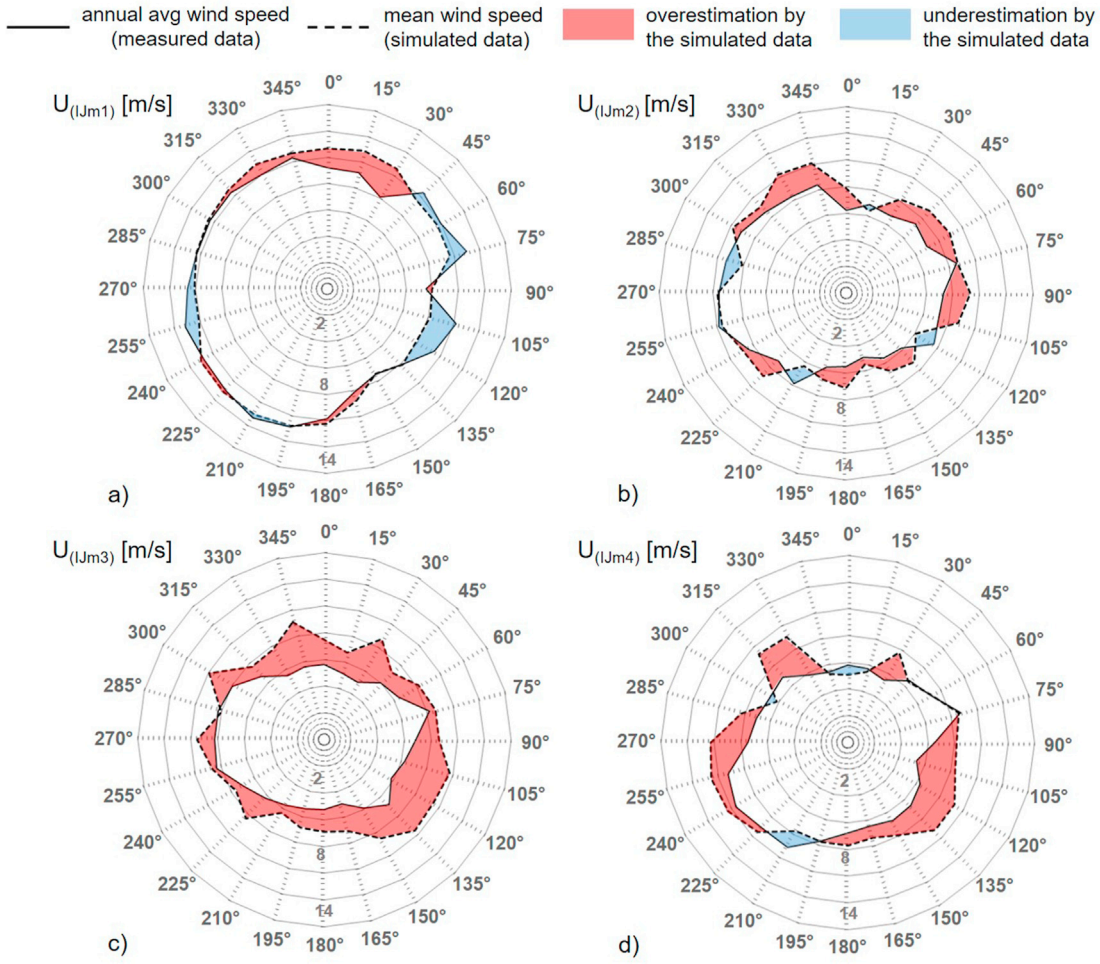

Fig. 20. Polar diagrams of the measured annual (July 2017–July 2018) average wind speed and computed wind speed at three positions (*IJm1*, *IJm2* and *IJm4*) with *IJm1* as reference position for the 24 reference wind directions (θ).

usually carried out in these areas also imply high risks for human beings. The consequences of accidents in seaport areas may be not only economic losses but also loss of human lives.

The size of seaport infrastructures as well as of container ships and cruise ships has increased significantly over the last decades. The increasing ship size does not only cause larger wind forces but also larger ship inertia, which renders the navigation through the port areas even more difficult, especially on windy days. In this regard, the knowledge of macroscale and microscale wind conditions is essential for safety management, for maneuvering and mooring of ships, for optimizing the harbor design and also for reducing economic losses associated with port disruption due to extreme wind events.

In this paper the reliability of the 3D steady RANS approach for predicting the microscale wind conditions in a seaport area is analyzed. The *IJmuiden sea lock*, in Netherlands, and the surrounding built environment is chosen as case study. Note that this study focused on specific seaport area located in Europe, but the same methodology could also be adopted for different complex urban environments worldwide, including – but not limited to - seaport areas and sea locks. At the time of writing this article, the *IJmuiden* sea lock is the largest in the world. The CFD simulations are carried out for 24 reference wind directions assuming neutral atmospheric conditions representative of strong winds. For CFD validation, four 2D ultrasonic anemometers were installed and measurements were performed from July 2017 to July 2018. The CFD simulation results are compared to the measurements in terms mean wind speed amplification factor, turbulence intensity amplification factor and local wind direction.

The present study is based on several assumptions:

- In absence of temperature data, possible neutral atmospheric stability conditions were selected based on the Pasquill stability classes considering only those events with a 10-min mean wind speed larger than 6 m/s. Future research can consider non-neutral atmospheric stability.
- The computational domain was constructed taking into account the *new* configuration of the *IJmuiden sea lock* (see Fig. 3) but on-site measurements were carried out on the *old* configuration, as explained in Section 3. This is expected to have contributed to the deviations between measurements and simulations.
- Due to the high complexity of the area under study, in accordance with several previous publications (as Carpentieri and Robins, 2015, Ricci et al., 2017 and 2020) geometrical simplifications were applied to the buildings, bridges, cranes, streets and canals in the *immediate proximity* and *surrounding* areas, as described in Section 4.1

Overall, the 3D steady RANS approach showed a sufficiently high reliability for predicting the wind conditions in the seaport area under neutral atmospheric conditions, in accordance with previous similar studies (e.g. Blocken et al., 2015; Ricci et al., 2020a). This is confirmed by the satisfactory agreement in terms of amplification factor and local wind

Fig. 21. Polar diagrams of measured and simulated local wind directions (ϕ), at four measuring positions (*IJm1*, *IJm2*, *IJm3* and *IJm4*) and for the 24 reference wind directions (θ).

direction between simulated and measured data. Conversely, a less satisfactory agreement was found in terms of turbulence intensity amplification factor, which is unsurprising given the limitations of steady RANS modeling. The largest deviations (i.e. greater than 30%) in terms of turbulence intensity amplification factor are found at the measuring positions in the middle of the sea lock where possible large sheltering effects occur due to the high surface roughness and the local-scale forcing effects, as also shown in previous studies (e.g. Oke 2002; Lin et al., 2014; Carpentieri and Robins 2015; Ricci et al., 2020b; Vita et al., 2020a and 2020b). Beyond the inability of the steady RANS approach in properly predicting the wind flow in separation zones, the deviations between simulated and measured data are possibly caused by the fact that the comparison was made for two different sea lock configurations (as previously mentioned), being the *old* versus the *new* configuration (Fig. 4).

This paper, in line with some other research projects carried out by the authors on different port areas, confirms that 3D steady RANS approach in combination with on-site measurements and wind-tunnel tests can be of great support for seaport stakeholders in predicting the microscale wind conditions. In particular, the validated results of 3D RANS approach can provide a clear overview about the wind flow pattern (Blocken et al., 2015), the wind experienced by the cruise ships and/or container ships in port areas especially when surrounded by a large variety of buildings and port infrastructures (Ricci et al., 2020), and also insight into the atmospheric boundary layer development throughout the whole area under study (Ricci et al. 2017, 2019). These results emphasize how the most common reference wind speed of 10 m/s (at 10 m MSL) or the logarithmic wind profile usually adopted by the majority of port stakeholders worldwide to calculate wind forces on moored ships and port infrastructures (by their homemade software), might not hold anymore in a such complex environment. However, despite the large amount of publications in atmospheric physics and wind engineering, a unitary approach to assess wind flow in port areas and wind forces on port infrastructures and ships is still missing.

Instead of the 3D steady RANS approach, more sophisticated numerical approaches could be explored, such as large eddy simulation (LES) or hybrid LES/unsteady RANS approaches. However, these require even more care for high-quality grid generation, more sophisticated boundary conditions and a much higher computational cost and time. While the RANS simulations can be based on extensive best practice guideline (BPG) documents that have been developed over the past decades, for the LES approach such extensive best practice advice is at this moment still largely missing, which is considered as a serious limitation for high-quality LES in wind engineering (Blocken, 2018).

A real-time software application aimed at providing local-scale wind conditions in seaport areas worldwide, based on CFD results and standard weather station recordings (as shown in this paper), is currently under development by the authors. The software will help the port stakeholders to recognize possible threats for the tugboat pilots when navigating ships through port areas and mooring ships under strong wind conditions.

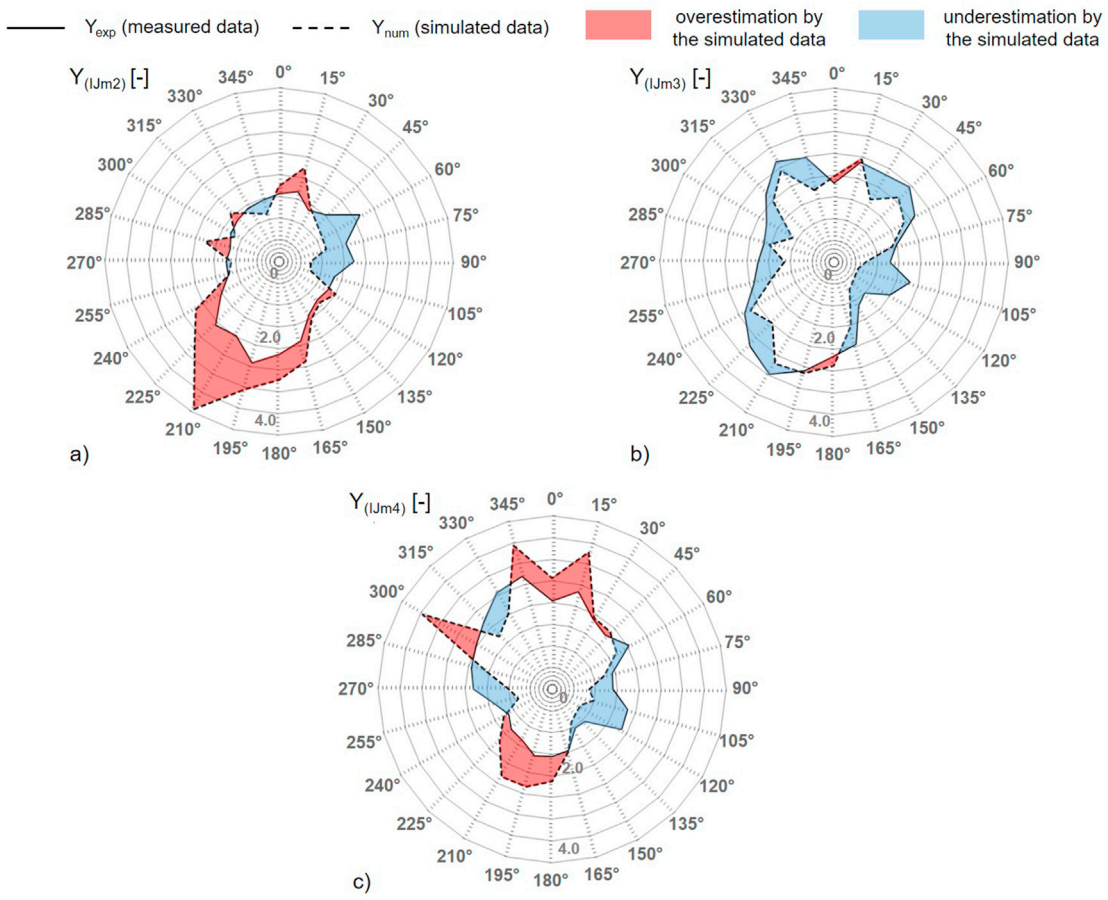

Fig. 22. Polar diagrams of measured and simulated turbulence intensity amplification factors (Y) values at three measurement positions for the 24 reference wind directions (θ).

CRediT authorship contribution statement

A. Ricci: Numerical and experimental investigations, data analysis, writing, data and text editing, revising. **B. Blocken:** Funding acquisition, supervising, data and text editing, revising.

Declaration of competing interest

The authors declare that they have no known competing financial interests or personal relationships that could have appeared to influence the work reported in this paper.

Acknowledgements

The authors gratefully acknowledge the Koninklijk Nederlands Meteorologisch Instituut (KNMI) and the Port Authority of Amsterdam for the collaboration. The authors also gratefully acknowledge the partnership with ANSYS CFD.

References

Al-Yahyai, S., Charabi, Y., Gastli, A., 2010. Review of the use of numerical weather prediction (NWP) models for wind energy assessment. Renew. Sustain. Energy Rev. 14, 3192–3198.
ANSYS Fluent, 2013. Release 16.0, Theory Guide. ANSYS Inc, Canonsburg.
Antoniou, N., Montazeri, H., Neophytou, M., Blocken, B., 2019. CFD simulation of urban microclimate: validation using high-resolution field measurements. Sci. Total Environ. 695, 133743.
Arslan, H., Baltaci, H., Oktay Akkoyunlu, B., Karanfil, S., Tayanc, M., 2020. Wind speed variability and wind power potential over Turkey: casestudies for Çanakkale and_ Istanbul. Renew. Energy 145, 1020–1032.
Baker, C.J., 2007. Wind engineering - past, present and future. J. Wind Eng. Ind. Aerod. 95, 843–870.
Becker, A.H., Matson, P., Fischer, M., Mastrandrea, M.D., 2015. Towards seaport resilience for the climate change adaptation: stakeholder perceptions of hurricane impacts in Gulfport (MS) and Providence (RI). Prog. Plann. 99, 1–49.
Blocken, B., 2018. LES over RANS in building simulation for outdoor and indoor applications: a foregone conclusion? Build. Simul. 11, 821–870.
Blocken, B., Vervoort, R., van Hooff, T., 2016. Reduction of outdoor particulate matter concentrations by local removal in semi-enclosed parking garages: a preliminary case study for Eindhoven city center. J. Wind Eng. Ind. Aerod. 159, 80–98.
Blocken, B., van der Hout, A., Dekker, J., Weiler, O., 2015. CFD simulation of wind flow over natural complex terrain: case study with validation by field measurements for Ria de Ferrol, Galicia, Spain. J. Wind Eng. Ind. Aerod. 147, 43–57.
Blocken, B., 2015. Computational Fluid Dynamics for Urban Physics: importance, scales, possibilities, limitations and ten tips and tricks towards accurate and reliable simulations. Build. Environ. 91, 219–245.
Blocken, B., 2014. 50 years of computational wind engineering: past, present and future. J. Wind Eng. Ind. Aerod. 129, 69–102.
Blocken, B., Gualtieri, C., 2012. Ten iterative steps for model development and evaluation applied to computational fluid dynamics for environmental fluid mechanics. Environ. Model. Software 33, 1–22.
Blocken, B., Stathopoulos, T., Carmeliet, J., 2007a. CFD simulation of the atmospheric boundary layer: wall function problems. Atmos. Environ. 41, 238–252.
Blocken, B., Carmeliet, J., Stathopoulos, T., 2007b. CFD evaluation of the wind speed conditions in passages between buildings – effect of wall-function roughness modifications on the atmospheric boundary layer flow. J. Wind Eng. Ind. Aerod. 95, 941–962.
Britter, R., Schatzmann, M., 2007. Model Evaluation Guidance and Protocol Document COST Action 732. COST Office Brussels, Belgium, ISBN 3-00-018312- 4.
Bucci, V., Marino, A., Mauro, F., Nabergoj, R., Nasso, C., 2016. On advanced ship evacuation analysis. Engineering Mechanics 2016. In: Zolotarev, I., Radolf, V. (Eds.), Engineering Mechanics, pp. 98–101.

Burlando, M., Tizzi, M., Solari, G., 2017a. Characteristics of downslope winds in the liguria region. Wind Struct. 24, 613–635.
Burlando, M., Romanic, D., Solari, G., Hangan, H., Zhang, S., 2017b. Field data analysis and weather scenario of a downburst event in Livorno, Italy on 1 October 2012. Mon. Weather Rev. 145, 3507–3527. https://doi.org/10.1175/MWR-D-17-0018.1.
Burlando, M., Pizzo, M., Repetto, M.P., Solari, G., De Gaetano, P., Tizzi, M., 2014. Short-term wind forecast for the safety management of complex areas during hazardous wind events. J. Wind Eng. Ind. Aerod. 135, 170–181.
Burlando, M., De Gaetano, P., Pizzo, M., Repetto, M.P., Solari, G., Tizzi, M., 2013. Wind climate analysis in complex terrain. J. Wind Eng. Ind. Aerod. 123, 349–362.
Burlando, M., Carassale, L., Georgieva, E., Ratto, C.F., Solari, G., 2007. A simple and efficient procedure for the numerical simulation of wind fields in complex terrain. Boundary-Layer Meteorol. 125, 417–439.
Cao, X., Siu Lee Lam, J., 2018. Simulation-based catastrophe-induced port loss estimation. Reliab. Eng. Syst. Saf. 175, 1–12.
Carpentieri, M., Robins, A.G., 2015. Influence of urban morphology on air flow over building arrays. J. Wind Eng. Ind. Aerod. 145, 61–74.
Casey, M., Wintergerste, T., 2000. Best Practice Guidelines, ERCOFTAC Special Interest Group on Quality and Trust in Industrial CFD. ERCOFTAC, Brussels.
Cassola, F., Burlando, M., 2012. Wind speed and wind energy forecasting through Kalman filtering of Numerical Weather Prediction model output. Appl. Energy 99, 154–166.
Castillo-Manzano, J.I., Lopez-Valpuesta, L., 2018. What does cruise passengers' satisfaction depend on? Does size really matter? Int. J. Hospit. Manag. 75, 116–118.
Cebeci, T., Bradshaw, P., 1997. Momentum Transfer in Boundary Layers. Hemisphere Publishing Corporation, New York, ISBN 0070103003.
Cho, H.S., Lee, J.S., Moon, H.C., 2018. Maritime risk in seaport operation: a cross-country empirical analysis with theoretical foundations. Asian J. Shipping and Logistics 34 (3), 245–252.
Darbra, R.M., Casal, J., 2004. Historical analysis of accidents in seaports. Saf. Sci. 42, 85–98.
Donateo, A., Gregoris, E., Gambaro, A., Merico, E., Giua, R., Nocioni, A., Contini, D., 2014. Contribution of harbour activities and ship traffic to PM2.5, particle number concentrations and PAHs in a port city of the Mediterranean Sea (Italy). Environ. Sci. Pollut. Control Ser. 21, 9415-9129.
Donatini, L., Vantorre, M., Verwilligen, J., Delefortrie, G., 2019. Description of hydro/meteo data in ship manoeuvring simulators: a survey on the state of the art. Ocean Eng. 189, 106344.
Eurostat Statistics Explained, 2020. Maritime Ports Freight and Passenger Statistics.
Fabiano, B., Currò, F., Reverberi, A.P., Pastorino, R., 2010. Port safety and the container revolution: a statistical study on human factor and occupational accidents over the long period. Saf. Sci. 48, 980–990.
Ferziger, J.H., Perić, M., 2002. Computational Methods for Fluid Dynamics, third ed. Springer-Verlag, ISBN 3-540-42074-6.
Fluent Inc, 2005. Fluent 6.2 User's Guide. Fluent Inc., Lebanon.
Franke, J., Hellsten, A., Schlünzen, H., Carissimo, B., 2007. Best Practice Guideline for the CFD Simulation of Flows in the Urban Environment. COST Office Brussels, ISBN 3-00-018312-4.
Gomez Paz, M.A., Camarero Orive, A., Gonzalez Cancelas, N., 2015. Use of the Delphi method to determine the constraints that affect the future size of large container ships. Marit. Pol. Manag. 42 (3), 263–277.
Hanjalic, K., 2005. Will RANS survive LES? A view of perspectives. J. Fluid Eng. 127, 831–839.
Hut, 2015. http://rolfhut.nl/2015/12/11/1-meter-zeespiegelstijging-26-miljoen-extra-nederlanders-onder-zeeniveau, 29.07.2020.
Janssen, W.D., Blocken, B., van Wijhe, H.J., 2017. CFD simulations of wind loads on a container ship: validation and impact of geometrical simplifications. J. Wind Eng. Ind. Aerod. 166, 106–116.
Janssen, W.D., Blocken, B., van Hooff, T., 2013. Pedestrian wind comfort around buildings: comparison of wind comfort criteria based on whole-flow field data for a complex case study. Build. Environ. 59, 547–562.
Jian, W., Liu, C., Siu Lee Lam, J., 2019. Cyclone risk and assessment for East Asian container ports. Ocean Coast Manag. 178, 104796.
Karava, P., Jubayer, C.M., Savory, E., 2011. Numerical modelling of forced convective heat transfer from inclined windward roof of an isolated low-rise building with application to photovoltaic/thermal systems. Appl. Therm. Eng. 31 (11–12), 1950–1963.
Kantamaneni, K., Gallagher, A., Du, X., 2019. Assessing and mapping regional coastal vulnerability for port environments and coastal cities. J. Coast Conserv. 23, 59–70.
Katinas, V., Marciukaitis, M., Markevicius, A., 2009. Current situation of the wind energy use and investigation of wind resources in the coastal region of the Baltic Sea in Lithuania. Renew. Sustain. Energy Rev. 13, 201–207.
Kron, W., Löw, P., Kundzewicz, Z.W., 2019. Changes in risk of extreme weather events in Europe. Environ. Sci. Pol. 100, 74–83.
Kron, W., 2013. Coasts: the high-risk areas of the world. Nat. Hazards 66, 1363–1382.
Launder, B.E., Spalding, D.B., 1974. The numerical computation of turbulent flows. Comput. Methods Appl. Mech. Eng. 3, 269–289.
Lin, M., Hang, J., Li, Y., Luo, Z., Sandberg, M., 2014. Quantitative ventilation assessments of idealized urban canopy layers with various urban layouts and the same building packing density. Build. Environ. 79, 152–167.
Lu, H.A., Yeh, J., 2019. The impact of using mega containerships on operation and management of shipping lines. Transport. J. 58 (1), 38–64.
Malchow, U., 2017. Growth in containership sizes to be stopped? Maritime Business Rev. 2 (3), 199–210.
Martin, J., Martin, S., Pettit, S., 2015. Container ship size and the implications on port call workload. Int. J. Shipp. Transp. Logist. (IJSTL) 7 (5), 553–569.
Mathias, L., Ludwig, P., Pinto, J.G., 2019. Synoptic-scale conditions and convection-resolving hindcast experiments of a cold-season derecho on 3 January 2014 in western Europe. Nat. Hazards Earth Syst. Sci. 19, 1023–1040.
McGranahan, G., Balk, D., Anderson, B., 2007. The rising tide: assessing the risks of climate change and human settlements in low elevation coastal zones. Environ. Urbanization 19, 17–37.
McIntosh, R.D., Becker, A., 2019. Expert evaluation of open-data indicators of seaport vulnerability to climate and extreme weather impacts for U.S. North Atlantic ports. Ocean Coast Manag. 180, 104911.
Merk, O., 2015. The Impact of Mega-Ships. OECD-Report.
Moonen, P., Dorer, V., Carmeliet, J., 2011. Evaluation of the ventilation potential of courtyards and urban street canyons using RANS and LES. J. Wind Eng. Ind. Aerod. 99, 414–423.
Mori, N., Takemi, T., 2016. Impact assessment of coastal hazards due to future changes of tropical cyclones in the North Pacific Ocean. Weather and Climat. Extremes 11, 53–69.
Nederlands Instituut voor Beeld en Geluid, 1953. Eerste beelden van de Stormramp (1953). https://www.youtube.com/watch?time_continue=6&v=XcX5wb1k9UM&feature=emb_title, 22.07.2020.
Oke, T.R., 2002. Boundary Layer Climates, second ed. Routledge.
Oner, Y., Ozcira, S., Bekiroglu, N., Senol, I., 2013. A comparative analysis of wind power density prediction methods for Çanakkale, Intepe region, Turkey. Renew. Sustain. Energy Rev. 23, 491–502.
Pasquill, F., 1961. The estimation of the dispersion of windborne material. Meteorol. Mag. 90, 33–49.
Population Reference Bureau, 2003. Ripple Effects: Population and Coastal Regions Measure Communication, 1875 Connecticut Ave., NW, Suite 520, Washington, DC 20009 USA.
Port of Amsterdam, 2018. https://www.portofamsterdam.com/en/news-item/adjustment-lock-passage-regime-ijmuiden, 29.07.2020.
Repetto, M.P., Burlando, M., Solari, G., De Gaetano, P., Pizzo, M., Tizzi, M., 2018. A web-based GIS platform for the safe management and risk assessment of complex structural and infrastructural systems exposed to wind. Adv. Eng. Software 117, 29–45.
Repetto, M.P., Burlando, M., Solari, G., De Gaetano, P., Pizzo, M., 2017. Integrated tools for improving the resilience of seaports under extreme wind events. Sustain. Cities Soc. 32, 277–294.
Ricci, A., Janssen, W.D., van Wijhe, H.J., Blocken, B., October 2020a. CFD simulation of wind forces on ships in ports: case study for the Rotterdam Cruise Terminal. J. Wind Eng. Ind. Aerod. 205, 104315.
Ricci, A., Kalkman, I., Blocken, B., Burlando, M., Repetto, M.P., 2020b. Impact of turbulence models and roughness height in 3D steady RANS simulations of wind flow in an urban environment. Build. Environ. 171, 106617.
Ricci, A., Burlando, M., Repetto, M.P., Blocken, B., 2019. Simulation of urban boundary and canopy layer flows in port areas induced by different marine boundary layer inflow conditions. Sci. Total Environ. 670, 876–892.
Ricci, A., Kalkman, I., Blocken, B., Burlando, M., Freda, A., Repetto, M.P., 2018. Large-scale forcing effects on wind flows in the urban canopy: impact of inflow conditions. Sustain. Cities Soc. 42, 593–610.
Ricci, A., Kalkman, I., Blocken, B., Burlando, M., Freda, A., Repetto, M.P., 2017. Local-scale forcing effects on wind flows in an urban environment: impact of geometrical simplifications. J. Wind Eng. Ind. Aerod. 170, 238–255.
Rodrigue, J.P., Notteboom, T., 2009. The terminalization of supply chains: reassessing the role of terminals in port/hinterland logistical relationships. Marit. Pol. Manag. 36 (2), 165–183.
Rong, H., Teixeira, A.P., Guedes Soares, C., 2019. Ship trajectory uncertainty prediction based on a Gaussian Process model. Ocean Eng. 182, 499–511.
Ronza, A., Lázaro-Touza, L., Carol, S., Casal, J., 2009. Economic valuation of damages originated by major accidents in port areas. J. Loss Prev. Process. Ind. 22, 639–648.
Shih, T.H., Liou, W.W., Shabbir, A., Zhu, J., 1995. A new k-ε eddy-viscosity model for high Reynolds number turbulent flows e model development and validation. Comput. Fluids 24, 227–238.
Solari, G., Burlando, M., Repetto, M.P., 2020. Detection, simulation, modelling and loading of thunderstorm outflows to design wind-safer and cost-efficient structures. J. Wind Eng. Ind. Aerod. 200, 104142.
Solari, G., Repetto, M.P., Burlando, M., De Gaetano, P., Parodi, M., Pizzo, M., Tizzi, M., 2012. The wind forecast for safety management of port areas. J. Wind Eng. Ind. Aerod. 104–106, 266–277.
Stathopoulos, T., 2002. The numerical wind tunnel for industrial aerodynamics: real or virtual in the new millennium? Wind Struct. 5, 193–208.
Stull, R.B., 1988. An Introduction to Boundary Layer Meteorology, first ed. Springer Netherlands, ISBN 978-94-009-3027-8.
Sun, X., Feng, X., Gauri, D.K., 2014. The cruise industry in China: efforts, progress and challenges. Int. J. Hospit. Manag. 42, 71–84.
Tamura, Y., Cao, S., 2012. International group for wind-related disaster risk reduction (IG-WRDRR). J. Wind Eng. Ind. Aerod. 104–106, 3–11.
Taramelli, A., Valentini, E., Sterlacchini, S., 2015. A GIS-based approach for hurricane hazard and vulnerability assessment in the Cayman Islands. Ocean Coast Manag. 108, 116–130.
Tominaga, Y., Mochida, A., Yoshie, R., Kataoka, H., Nozu, T., Yoshikawa, M., Shirasawa, T., 2008. AIJ guidelines for practical applications of CFD to pedestrian wind environment around buildings. J. Wind Eng. Ind. Aerod. 96 (10–11), 1749–1761.
Torre, S., Burlando, M., Repetto, M.P., Ruscelli, D., 2019. Aerodynamic Coefficients on Moored Ships. Proceeding of the 15th International Conference on Wind Engineering, Beijing, China, September, pp. 1–6.

Ulbrich, U., Leckebusch, G., Donat, M., 2013. Windstorms, the most costly natural hazard in Europe. In: Boulter, S., Palutikof, J., Karoly, D., Guitart, D. (Eds.), Natural Disasters and Adaptation to Climate Change. Cambridge University Press, Cambridge, pp. 109–120.

UNCTAD, 2018. http://unctadstat.unctad.org/wds/ReportFolders/reportFolders.aspx, 29.07.2020.

UNCTAD/RTM, 2018. In: United Conference on Trade and Development. Review of Maritime Transport, ISBN 978-92-1-112928-1.

van Hassel, E., Meersman, H., Van De Voorde, E., Vanelslander, T., 2016. Impact of scale increase of container ships on the generalised chain cost. Marit. Pol. Manag. 43 (2), 192–208.

van Druenen, T., van Hooff, T., Montazeri, H., Blocken, B., 2019. CFD evaluation of building geometry modifications to reduce pedestrian-level wind speed. Build. Environ. 163, 106293.

van Hooff, T., Blocken, B., 2010. Coupled urban wind flow and indoor natural ventilation modelling on a high-resolution grid: a case study for the Amsterdam ArenA stadium. Environ. Model. Software 25, 51–65.

Vairetti, C., González-Ramírez, R.G., Maldonado, S., Álvarez, C., Voβ, S., 2019. Facilitating conditions for successful adoption of inter-organizational information systems in seaports. Transport. Res. Part A 130, 333–350.

Venkatram, A., 1996. An examination of the Pasquill-Gifford-Turner dispersion scheme. Atmos. Environ. 30, 1283–1290.

Versteeg, H.K., Malalasekera, W., 2007. An Introduction to Computational Fluid Dynamics: the Finite Volume Method. Harlow-Longman Scientific & Technical, London.

Vita, G., Shu, Z., Jesson, M., Quinn, A., Hemida, H., Sterling, M., Baker, C., 2020a. On the assessment of pedestrian distress in urban winds. J. Wind Eng. Ind. Aerod. 203, 104200.

Vita, G., Hashmi, S.A., Salvadori, S., Hemida, H., Baniotopoulos, C., 2020b. Role of inflow turbulence and surrounding buildings on large eddy simulations of urban wind energy. Energies 13 (19), 5208.

Walsh, K.J.E., McInnes, K.L., McBride, J.L., 2012. Climate change impacts on tropical cyclones and extreme sea levels in the South Pacific – a regional assessment. Global Planet. Change 80–81, 149–164.

Wang, P., Wang, F., Chen, Z., 2020. Investigation on aerodynamic performance of luxury cruise ship. Ocean Eng. 213, 107790.

Wang, J., Wan, D., 2020. CFD study of ship stopping maneuver by overset grid technique. Ocean Eng. 197, 106895.

Wieringa, J., 1992. Updating the Davenport roughness classification. J. Wind Eng. Ind. Aerod. 41–44, 357–368.

Yang, A.S., Su, Y.M., Wen, C.Y., Juan, Y.H., Wang, W.S., 2016. Estimation of wind power generation in dense urban area. Appl. Energy 171, 213–230.

Yip, T.L., 2008. Port traffic risks – a study of accidents in Hong Kong waters. Transport. Res. Part E 44, 921–931.

Zhang, Y., Lam Siu Lee, J., 2015. Estimating the economic losses of port disruption due to extreme wind events. Ocean Coast Manag. 116, 300–310.